
POTSDAM-INSTITUT FÜR KLIMAFOLGENFORSCHUNG

# Changes in North Atlantic Atmospheric Circulation in a Warmer Climate Favor Winter Flooding and Summer Drought over Europe

E. ROUSI,[a,e] F. SELTEN,[b] S. RAHMSTORF,[a,c,f] AND D. COUMOU[d,b,a,g]

[a] *Potsdam Institute for Climate Impact Research (PIK), Member of the Leibniz Association, Potsdam, Germany*
[b] *Royal Netherlands Meteorological Institute (KNMI), De Bilt, Netherlands*
[c] *Institute of Physics and Astronomy, University of Potsdam, Potsdam, Germany*
[d] *Institute for Environmental Studies, Vrije Universiteit (VU) Amsterdam, Amsterdam, Netherlands*

(Manuscript received 1 May 2020, in final form 15 December 2020)

ABSTRACT: Changes in atmospheric circulation under increasing greenhouse gas concentrations are important because of their implications for weather extremes and associated societal risks. However, uncertainties in models and future projections are still large and drivers behind circulation changes are not well understood. Particularly for Europe, a potential weakening of the Atlantic meridional overturning circulation (AMOC) is considered important as it affects SST patterns and ocean–atmosphere heat fluxes and, subsequently, European climate. Here we detect and characterize changes in atmospheric circulation patterns over the North Atlantic under increasing $CO_2$ concentrations in simulations of a very high-resolution, fully coupled climate model (CM2.6) with a realistic representation of the AMOC. We use an objective clustering technique (self-organizing maps) and validate the model's clusters against reanalysis data. We compare the frequency of those patterns in a $CO_2$ doubling experiment, characterized by an AMOC decline, with those in a preindustrial run, and find statistically significant changes. The most robust findings are 1) a ~30% increase in zonal flow regimes in February, relevant for flood risk in northwestern Europe, and 2) a ~60% increase in anticyclonic (high pressure) circulation directly west of the United Kingdom in August, relevant for western and central European drought. A robust decrease in the frequency of Scandinavian blocking is also seen across most months and seasons. Despite the uncertainties regarding atmospheric circulation response to climate change, our findings contribute to the increasing evidence for the emergence of robust high-impact changes over Europe.

KEYWORDS: North Atlantic Ocean; Atmospheric circulation; Climate change; Climate classification/regimes; General circulation models; Europe; Teleconnections

## 1. Introduction

In a warming world, a simple shift of the temperature distribution toward warmer values leads to a strong increase in hot extremes. Also, based on the Clausius–Clapeyron equation, we can expect more extreme precipitation, as every degree of warming increases atmospheric water holding capacity by 7% (Coumou and Rahmstorf 2012). With warming, more precipitation occurs as rain instead of snow and snow melts earlier in the year. Those factors combined lead to increased runoff and risk of flooding in late winter/early spring, but also to enhanced risk of drought in summer, especially over the continents (Trenberth 2011).

On a global scale, a poleward expansion of the tropics, with an accompanying shift of the subtropical dry zones, midlatitude jets, and storm tracks, has been detected over the past few decades (Vallis et al. 2015; Molnos et al. 2017; Perlwitz et al. 2017). This is corroborated by model-based studies showing this poleward shift under simulations with increasing $CO_2$ (Chang et al. 2012; Barnes and Polvani 2013). Further, summer circulation, in terms of the zonal-mean zonal wind, eddy kinetic energy (EKE), amplitude of transient Rossby waves (Coumou et al. 2015), and extratropical cyclone activity (Chang et al. 2016) has weakened over the past 40 years. Climate models project a similar amount of boreal summer circulation weakening under strong greenhouse gas forcing.

The North Atlantic is a particularly challenging region with a distinctive atmospheric and oceanic variability that plays an important role in shaping weather and climate over Europe (Woollings 2010). Considerable changes have been documented during the last decades across the North Atlantic climate system, including in the atmosphere, ocean, and cryosphere (Robson et al. 2018). Particularly for the period 2005–16, Robson et al. (2018) document an increase in the speed of the North Atlantic jet stream in winter and a southward shift of its location in summer, associated with a weakening summer North Atlantic Oscillation (NAO). In response to anthropogenic greenhouse gas forcing in models, the winter North Atlantic storm track is expected to strengthen and extend farther east, especially on its southern flank (Ulbrich et al. 2008). Moreover, a feature observed in all seasons but more pronounced in winter is a cooling of sea surface temperatures (SSTs) in the North Atlantic subpolar gyre, despite an overall

Supplemental information related to this paper is available at the Journals Online website: https://doi.org/10.1175/JCLI-D-20-0311.s1.

[e] ORCID: https://orcid.org/0000-0003-3191-2793.
[f] ORCID: https://orcid.org/0000-0001-6786-7723.
[g] ORCID: https://orcid.org/0000-0003-2155-8495.

*Corresponding author*: E. Rousi, rousi@pik-potsdam.de

DOI: 10.1175/JCLI-D-20-0311.1

global warming pattern (Rahmstorf et al. 2015). Model simulations (Stouffer et al. 2006), SST fingerprint analyses (Caesar et al. 2018), a salinity increase in the subtropical Atlantic (Zhu and Liu 2020), a long-term slowdown of the Florida Current (Piecuch 2020), and recent direct measurements from the RAPID project (Robson et al. 2014) suggest that this feature is the result of a slowdown of the Atlantic meridional overturning circulation (AMOC). The spatial cooling pattern seen in the North Atlantic can be explained by such a slowdown, which causes a reduced northward heat transport and a northward shift of the Gulf Stream (Caesar et al. 2018). Recent work has indeed formally attributed the warming hole over the North Atlantic to anthropogenic greenhouse gas forcing (Chemke et al. 2020; Keil et al. 2020). Links between the AMOC and the variability in the North Atlantic SSTs and atmospheric circulation that affects European climate have been found both in models (Latif et al. 2019) and observations (Josey et al. 2018), but the exact processes are complex and poorly understood (Allan and Allan 2019), while there is evidence that models do not adequately capture such links and their causal chains (Simpson et al. 2018). For summer, Haarsma et al. (2015) used state-of-the-art global climate model experiments and observations and showed that the projected higher pressure over the British Isles is part of an atmospheric response to a decelerating AMOC. Duchez et al. (2016) found that a cold SST anomaly over the North Atlantic was present prior to the most extreme heatwaves in central Europe since the 1980s. Physically, the ocean cold anomaly and associated changes in SST gradients trigger a quasi-stationary Rossby wave response that favors high pressure and warm temperature anomalies over Europe.

Europe has indeed seen some high-impact weather extremes in recent years, both in winter (Kretschmer et al. 2017, 2018) and summer (Russo et al. 2014; Kornhuber et al. 2019), and its exposure to climate-related multiple hazards is expected to see a progressive and strong increase under ongoing climate change (Forzieri et al. 2016). This is particularly evident with extremely hot summers and intense heatwaves over Europe (Christidis and Stott 2015b; Russo et al. 2015). Soil moisture–temperature feedbacks (Seneviratne et al. 2010) that can amplify temperature extremes (Vogel et al. 2017) and/or changes in circulation might play an important role in this overproportional increase in European heatwaves (Horton et al. 2015; Coumou et al. 2018; Suarez-Gutierrez et al. 2020). The intensity of some recent such heatwaves, like in the summer of 2018 (Kornhuber et al. 2019), is difficult to explain on the basis of the direct long-term warming effect of greenhouse gas forcing alone (Schär et al. 2004; Coumou et al. 2018). Climate models show smaller trends than observed with fewer really severe heatwaves (van Oldenborgh et al. 2019). Anomalous atmospheric circulation patterns, such as a meandering jet stream, have been linked to extreme summer weather in different regions of the Northern Hemisphere midlatitudes. Such events are interconnected via circumglobal high-amplitude Rossby waves that show preferred geographical positions and constitute recurrent atmospheric circulation patterns in summer (Röthlisberger and Martius 2019; Teng and Branstator 2019; Kornhuber et al. 2020).

Among the most illustrative examples of large-scale circulation–induced climate extremes during the cold season is the record average rainfall in the United Kingdom in winter 2013/14 that led to extensive and prolonged flooding. This exceptional rainfall was the result of a persistent sequence of low pressure systems passing over or close to the British Isles (Christidis and Stott 2015a), propagating along a very strong zonally oriented North Atlantic jet stream. This generated numerous damaging windstorms in many areas across western Europe (Knight et al. 2017). In that winter, the frequency of zonal regimes in January was the highest since 1871 (Schaller et al. 2016) and the excess rainfall has been attributed to human-induced changes of both dynamical and thermodynamical nature (Vautard et al. 2016). Two years later, the 2015/16 winter brought another extreme hydrological episode in the United Kingdom, in terms of magnitude, duration, spatial extent, and impacts, adding to an apparent cluster of flood events in the early twenty-first century (Barker et al. 2016). Blöschl et al. (2019) demonstrated that increasing autumn and winter rainfall has resulted in increasing floods in northwestern Europe in the past five decades, with the northern United Kingdom being one of the hotspots. Increases in extreme precipitation in northwestern Europe are in turn related to the poleward shifts of the subpolar jet and storm tracks observed since the 1970s, which have been associated with more prevalent positive phases of the NAO (IPCC 2013).

Changes in atmospheric circulation are primarily controlled by the dynamics of large-scale atmospheric motions and strongly project on regional climate, while our understanding of them is still limited, comprising high levels of uncertainty (Shepherd 2014). Previous studies have mainly focused on changes in the mean flow, looking at different properties of atmospheric circulation, such as sea level pressure, wind, or storm tracks, thus not accounting for the full variability. One way to study and quantify changes there in atmospheric circulation is the use of weather regimes (Vautard 1990; Michelangeli et al. 1995; Cassou et al. 2004) that capture an important share of atmospheric variability in a handful of dominant patterns, thereby reducing dimensionality. The purpose of the present study is to analyze changes in atmospheric circulation patterns, or weather regimes, over the North Atlantic sector associated with increasing $CO_2$ in a high-resolution coupled climate model experiment. The circulation patterns are defined using self-organizing maps (SOMs), an objective topology-preserving clustering algorithm based on neural networks (Kohonen 2013), which has been extensively used to study atmospheric circulation in the recent decades (Sheridan and Lee 2011; Skific and Francis 2012; Lee et al. 2017; Rousi et al. 2020). We validate the modeled atmospheric circulation patterns against reanalysis data and examine changes in frequency of occurrence, as well as in their spatial structure, between the preindustrial and the $2 \times CO_2$ run. We find that there are significant changes in frequency that exceed the internal variability of the model, which are impact-relevant and are consistent with previous findings regarding changes in the mean flow. The novelty of this work consists in the combination of a validated very high-resolution model (GFDL CM2.6), an objective method of defining patterns of atmospheric

variability (SOMs), and a systematic study of changes therein on a monthly basis. The choice of the model was based on its realistic representation of the ocean circulation (Griffies et al. 2015), which is a key contributor to expected future atmospheric circulation changes (Woollings et al. 2012; Haarsma et al. 2019).

## 2. Data and methods

### a. Data

In this study we use data from two simulation runs of the CM2.6 coupled global climate model, which was developed at the Geophysical Fluid Dynamics Laboratory (GFDL) of the National Oceanic and Atmospheric Administration (NOAA). CM2.6 has a resolution of 0.1° (10 km) for the ocean and 0.5° (50 km) for the atmosphere. The ocean contains 50 vertical levels and a sea ice model. The very high resolution over the ocean provides a more realistic simulation of the Gulf Stream and the AMOC compared to coarser models, reducing regional SST biases and resolving mesoscale ocean eddies (Griffies et al. 2015). In particular, this model eliminates the bias in the separation point of the Gulf Stream from the coastline of the United States, which is common in coarser models (Caesar et al. 2018). For instance, for phase 5 of the Coupled Model Intercomparison Project (CMIP5), other versions of GFDL models were used (CM2.1 and CM3), which had a much lower resolution both over ocean and atmosphere (Delworth et al. 2012). Therefore, the added value of CM2.6 is due to the particularly fine ocean and atmosphere resolution. The importance of fine model resolution in the representation of weather regimes is pointed out by Dawson et al. (2012), who compared two models of different resolution and found a more realistic representation in the finer one. Similarly, Fabiano et al. (2020) reported that state-of-the-art coupled climate models from the PRIMAVERA project are better at reproducing the observed Euro-Atlantic weather regimes than their predecessors and that there is some evidence that this is due to increased model resolution. More generally, the eddy feedback on the mean flow, poleward heat fluxes, and frontal structures have all shown to be strongly affected by an increase in horizontal resolution in recent studies (Czaja et al. 2019).

The two simulations of the CM2.6 model used here have been initialized from present-day ocean conditions, followed by a spinup time of 100 years at constant 1860 $CO_2$ concentrations (Saba et al. 2016):

1) An 80-yr run with stable $CO_2$ concentrations fixed at preindustrial level as for year 1860 (PI), and
2) an 80-yr run in which $CO_2$ increases by 1% per year over 70 years until its concentration doubles and then remains stable for the last 10 ($2 \times CO_2$). By the end of this run, the AMOC strength has weakened by about 3 Sv ($1\,\text{Sv} \equiv 10^6\,\text{m}^3\,\text{s}^{-1}$) (see also top panel of Fig. 1).

To study patterns of atmospheric circulation, we use the streamfunction at the 250-hPa pressure level ($\psi 250$) from the two model runs. The streamfunction is connected to the wind via the following equations:

$$u = -\frac{\partial \psi}{\partial y}, \quad \text{and} \tag{1}$$

$$v = \frac{\partial \psi}{\partial x}, \tag{2}$$

where $\psi$ is the streamfunction, and $u$ is the zonal and $v$ the meridional component of the wind.

We chose the streamfunction, following Branstator (2002) and Branstator and Selten (2009), instead of geopotential height at a certain pressure level, because the latter is readily affected by the tropospheric warming due to increasing $CO_2$, and encompasses trends that makes the interpretation in terms of changes in circulation more difficult. By using streamfunction we avoid this complication. To validate the model data for the control run period, we use the ERA-Interim reanalysis dataset for the 40-yr period 1979–2018 (Dee et al. 2011). For all datasets we calculate 5-day means from the daily fields in order to eliminate transient disturbances and weather noise. The geographical domain employed for the definition of the weather regimes is a broader area above the Euro-Atlantic region (30°–70°N, 80°W–40°E). For the validation, we compare both the climatology of model and reanalysis and the SOM clusters of the two. For the SOM clustering we use raw data and we do not calculate anomalies or detrend the data, as we do not want to mask the signal and the spatial patterns that occur due to the increase of the $CO_2$. To assess the differences in atmospheric patterns under increased $CO_2$ concentrations, we only use the last 40 years of the transient simulation, where the changes are more pronounced. Finally, we look at total precipitation data from the same two runs to examine the impacts of the circulation changes.

### b. Self-organizing maps

In this paper we use self-organizing maps (SOMs; Kohonen 2013) in order to obtain various patterns of atmospheric variability. The SOMs method is a machine learning iterative technique that consists of a topological ordering algorithm and has been widely used in many different fields in the recent decades. Its popularity is due to several advantages compared to other traditional clustering algorithms. First, the topological ordering of the clusters can be useful as it provides a nonlinear distribution of overlapping, nondiscreet continuum of states, instead of discrete realizations as is the case with principal component analysis and its orthogonal constraint (Hewitson and Crane 2002). Furthermore, each of the final clusters contains information not only from the data that are grouped within it, but also from the whole data distribution, by incorporating a neighborhood function that declines iteratively. As the final clusters, or SOM nodes, are topologically ordered in a two-dimensional array, the intracluster relationships are better represented and easier to visualize. Therefore, compared to more traditional clustering techniques, such as $k$-means or hierarchical clustering, SOMs provide a better representation of the intra- and intercluster relationships of the input data. Moreover, as a machine learning neural network–based technique, SOMs are able to learn from the data and thus benefit from large datasets to find the underlying patterns (Richardson et al. 2003). Apart from main modes of variability,

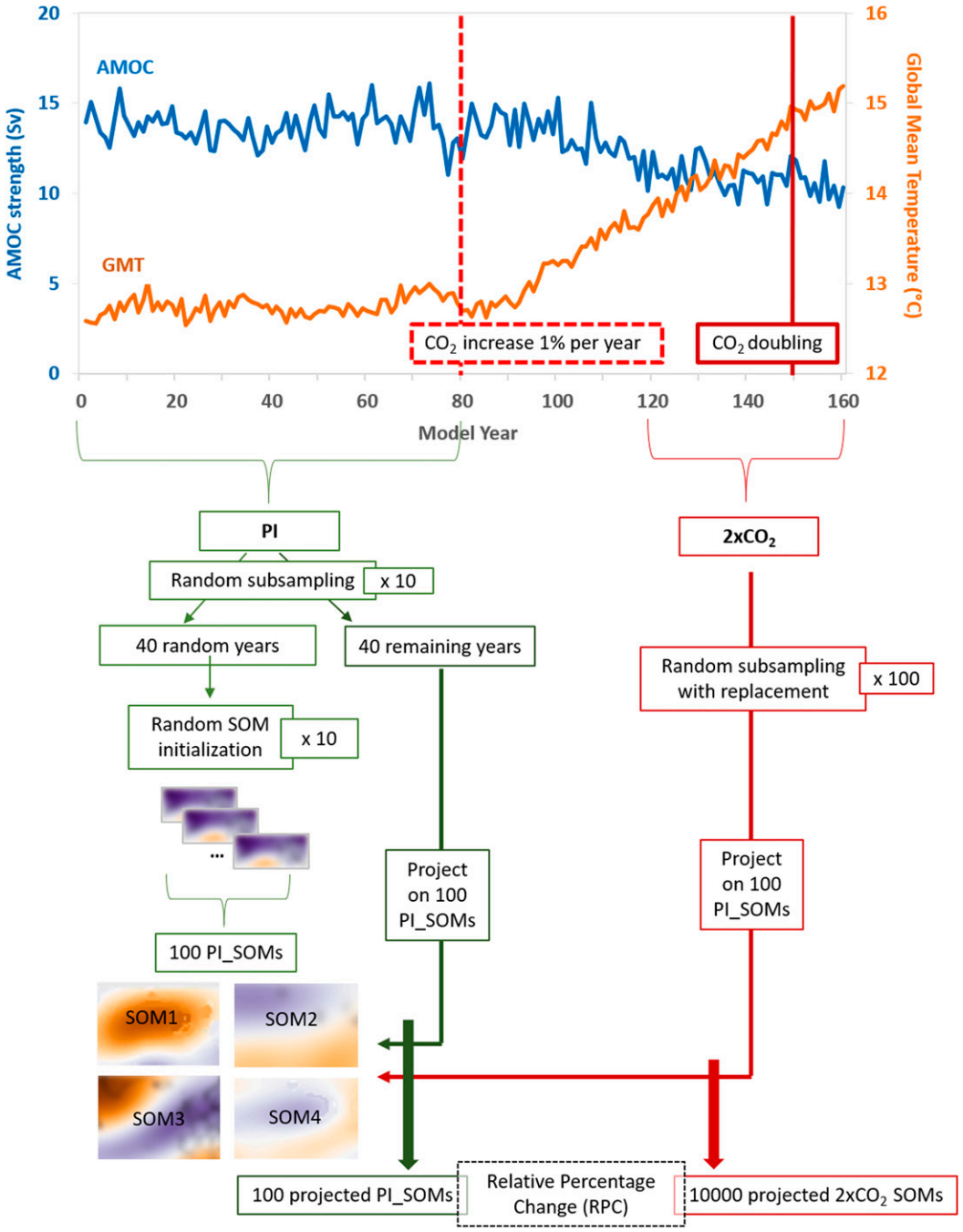


FIG. 1. Description of model runs and methodology. The graph at the top shows the AMOC strength (Sv; blue line), the global mean temperature (°C; orange line), and the $CO_2$ concentration changes in the two model runs, PI and 2 × $CO_2$. Underneath, the subsampling, the SOM clustering, and the projection of the data are described.

SOMs have been found useful in depicting transitional states (Hewitson and Crane 2002; Sheridan and Lee 2011; Rousi et al. 2015) and nonlinear aspects of variability (Reusch et al. 2007; Gervais et al. 2020). For all these reasons, SOMs have been increasingly used in studies regarding atmospheric circulation patterns, their variability, and changes therein, not only over the North Atlantic domain (Reusch et al. 2007; Gervais et al. 2020) but also in various other regions around the world [e.g., the Northern Hemisphere midlatitudes (Horton et al. 2015; Lee et al. 2017), North America (Francis et al. 2018), the Middle East (Luong et al. 2020), East Asia (Wang et al. 2015), Africa (Guèye et al. 2012; Quagraine et al. 2019), the Southern

Hemisphere (Chang and Johnson 2015), Australia (Alexander et al. 2010), etc.].

One of the choices that has to be made a priori in SOMs is the number of clusters to be used, or the size of the SOM array. This should be a compromise between a number that is large enough to capture the physical characteristics of the data but still small enough so that the clusters are well separated among them (Lee et al. 2017). A way to measure how well the clusters are separated is the so-called variance ratio, which is the ratio between the intercluster and the intracluster distances. The larger the variance ratio the better separated and compact are the clusters (Fabiano et al. 2020). Moreover, a relatively small number of patterns remains manageable as dimensionality is reduced. Here, we tried different numbers of SOMs and decided to keep four (in a $2 \times 2$ SOM array), which matches the number of North Atlantic weather regimes commonly identified in the literature (Kimoto and Ghil 1993; Michelangeli et al. 1995; Yiou and Nogaj 2004). For consistency and to facilitate comparison among months we choose to use four SOMs for all months. This is optimal for winter but may not be so for summer when the higher spatial variability of the atmospheric circulation makes it more difficult to identify a set of fixed patterns/weather regimes, as discussed in Cortesi et al. (2019). Nevertheless, we find that robust changes in summer atmospheric circulation patterns are consistent among four and six SOMs (not shown) and thus we choose to continue the analysis for four SOMs in all months.

The SOM training process starts with a random initialization of the initial weight vectors. Then, some random input data vector $\mathbf{x}$ is selected and the best matching unit (BMU) for it is chosen based on the minimum distance, using a distance metric such as the Euclidean distance that was used here. After this step, the BMU ($c_k$) is updated, becoming more similar to the input data vector that was just assigned to it, according to a learning rate parameter $\alpha$ and the following update function:

$$c_k(t+1) = c_k(t) + \alpha(t) \times h_{ck}(t) \times [\mathbf{x}(t) - c_k(t)], \qquad (3)$$

where $\alpha$ is the learning rate parameter that decreases with each iteration ($t$), and $h_{ck}$ a neighborhood function, which determines how many SOM nodes surrounding the updated SOM will be affected. Here, the bubble type neighborhood function was used:

$$h_{ck}(t) = F[\sigma(t) - d_{ck}], \qquad (4)$$

where $\sigma$ is the neighborhood radius that decreases with iteration ($t$), $d_{ck}$ is the Euclidean distance between the BMU $c$ and another one of the SOM nodes $k$, and $F(x)$ is a step function that takes the value 1 as long as the neighborhood radius remains larger than the Euclidean distance and the value 0 when the radius becomes equal to it.

After this step the whole process is repeated as long as the final SOM nodes keep changing, which leads to the finalization of the SOM array when all input data have been classified to their BMU.

To account for the uncertainty introduced by the random initialization of the SOM algorithm (Fort et al. 2002), we ran 100 randomly initialized SOMs of our PI data for each month and use their mean composites as our four weather regimes and the full distribution of their frequencies. This way we make sure that the random initialization does not influence the robustness of our clusters. To apply the SOM algorithm we used the latest version of the "kohonen" package in R (Wehrens and Kruisselbrink 2018).

### c. *Changes in atmospheric circulation patterns and their impacts*

To assess the changes in patterns of atmospheric variability under a climate change scenario we follow the steps described below for each month separately (see also Fig. 1):

1) We perform SOM clustering on 10 sets of 40 randomly selected years of the PI. By using several subsamples of 40 random years from the PI we account for the uncertainty that may be introduced to our results due to internal variability in the model data. For each of the 10 random subsamples we perform 10 random SOM initializations to account for the methodological uncertainty and obtain robust clusters. By the end of this step, we have 100 sets of four SOMs, corresponding to four weather patterns, for each month. The composites presented in the Results regarding the model validation are the mean SOMs of all the 100 iterations for each weather pattern and month (see Figs. 3 and 4). We also get a full distribution of the frequencies for each of those patterns ($F_{\mathrm{PI}}$) and a distribution of Euclidean distances ($D_{\mathrm{PI}}$). The latter show the distance of the input data to their best matching unit, which is the SOM they have been assigned to. Those intracluster distances provide a metric of how uniform the clusters are. The Euclidean distance is calculated as shown in Eq. (5) and it is the same metric used by the SOM algorithm in order to assign data units to the SOM clusters:

$$d_i = \sqrt{\sum_{i=1}^{N} (\boldsymbol{\psi}_i - \mathbf{c}_k)^2}, \qquad (5)$$

where $\boldsymbol{\psi}_i$ is the vector of streamfunction at 250 hPa for each of the input data $i$ and $\mathbf{c}_k$ is the vector of the centroid of each of the four SOMs ($1 < k < 4$).
2) Then we project the 40 remaining years of the PI from each of the 10 random subsamples on the 100 SOM sets. This is done by assigning each of the remaining data to one of the four SOM clusters, according to the minimum Euclidean distance from their centroids. We call these new 100 sets projected PI_SOMs. After this step, we have obtained the respective mean spatial pattern of the projected PI_SOMs, a distribution of their frequencies ($F_{\mathrm{projPI}}$) and a distribution of their Euclidean distances from the SOM centroid ($D_{\mathrm{projPI}}$).
3) Similarly, we project 100 random subsamples of 40 years with replacement from the $2 \times CO_2$ data on the 100 PI SOMs, again with the use of Euclidean distance and we obtain the so-called projected $2 \times CO_2$_SOMs. Each of those is similarly characterized by the mean

spatial pattern, a distribution of frequencies ($F_{2\times CO_2}$) and a distribution of Euclidean distances from the SOM centroid ($D_{2\times CO_2}$).

4) Then we compare the frequency distributions of the two projected sets of SOMs, PI and 2 × $CO_2$, in order to examine whether there are differences in the double $CO_2$ experiment that exceed the natural and decadal variability of the model during the period of stable preindustrial $CO_2$ concentrations. We calculate the relative percentage change (RPC) between the mean frequency of the patterns as follows:

$$\mathrm{RPC} = \frac{f_{2\times \mathrm{CO2}} - f_{\mathrm{projPI}}}{f_{\mathrm{projPI}}} \times 100\%, \tag{6}$$

where $f_{2\times CO_2}$ is the mean frequency for each pattern of the projected 2 × $CO_2$_SOMs and $f_{\mathrm{projPI}}$ is the mean frequency for each pattern of the projected PI_SOMs. The 95% confidence interval of the relative change is also presented.

We also compare the empirical cumulative distributions (ECDFs) of the Euclidean distances from the SOM centroid between PI and 2 × $CO_2$ SOMs. We test the difference in the distributions with the Kolmogorov–Smirnoff test and we present the ks statistic, which is the maximum absolute distance between the two ECDFs.

5) Finally, we calculate the percentage of emerging patterns in the 2 × $CO_2$, which we define as the data that exceed the outer boundary of a SOM. We consider the outer boundary to be the maximum Euclidean distance of the projected PI SOM data from the respective PI SOM centroid. Therefore, all the 2 × $CO_2$ data falling outside this threshold are considered emerging.

Following this methodological approach, we achieve a fair comparison between two projected sets of SOMs, without using the data that were used to define our ''original'' SOMs. We also account for internal and multidecadal variability of the model data and for methodological uncertainties. In section 3 we present in detail a winter and a summer month, February and August; results for all months are presented in the online supplemental material.

As a final step, in order to examine the impacts of the changes in atmospheric circulation patterns on the precipitation regime over Europe, we first projected the mean SOMs that were defined as described in the previous section on the PI and 2 × $CO_2$ data, in order to assign each 5-day mean to its most similar SOM (based on the minimum Euclidean distance from the SOM centroids) and create a calendar of SOMs. Then, we looked at composites of total precipitation for February and August for the particular SOMs that showed significant changes. We separated the thermodynamical (related to the fact that the 2 × $CO_2$ run represents a warmer world) and dynamical (related to the changes in frequency of the weather regimes) effect on precipitation using the following equations:

$$\Delta P_{\mathrm{total}} = (P_{2\times CO_2} \times f_{2\times CO_2}) - (P_{\mathrm{PI}} \times f_{\mathrm{PI}}), \tag{7}$$

$$\Delta P_{\mathrm{thermo}} = (P_{2\times CO_2} - P_{\mathrm{PI}}) \times f_{\mathrm{PI}}, \tag{8}$$

$$\Delta P_{\mathrm{dyn}} = \Delta P_{\mathrm{total}} - \Delta P_{\mathrm{thermo}}, \tag{9}$$

where $\Delta P_{\mathrm{total}}$ is the total change in precipitation between 2 × $CO_2$ and PI for a certain SOM pattern, $P_{2\times CO_2}$ ($P_{\mathrm{PI}}$) is the composite of precipitation for the SOM pattern in the 2 × $CO_2$ (PI) run expressed in anomalies from the PI monthly climatology (in mm per 5-day mean), and $f_{2\times CO_2}$ ($f_{\mathrm{PI}}$) is the frequency of this SOM pattern in the 2 × $CO_2$ (PI) run expressed in units of 5-day means. Also, $\Delta P_{\mathrm{thermo}}$ represents the thermodynamical effect, and thus the change in precipitation if no change in frequency occurs; $\Delta P_{\mathrm{dyn}}$ shows the dynamical effect introduced by the change in frequency of a certain SOM pattern between 2 × $CO_2$ and PI.

Finally, we looked at changes in the length of dry spells for August. We define a dry spell as a period of five consecutive days that had very little precipitation. Different precipitation thresholds can be used, depending mainly on the region and the scope of the study. Here, we chose a threshold of precipitation less than 1 mm, following different previous studies focusing on the European domain (Huth et al. 2000; Moberg and Jones 2005).

## 3. Results

### a. *Model validation*

For the validation of the model, we first compare the climatological wind speed between the preindustrial run of the model (PI) and the reanalysis data (ERA-Interim, herein ERAInt). Figure 2 shows the climatology of wind speed at 250 hPa for ERAInt (Figs. 2a,d) and the PI of the model (Figs. 2b,e), as well as the differences between the two (Figs. 2c,f). The results are presented here only for February and August (see Fig. S1 in the online supplemental material for the climatological zonal mean wind profiles for all months). We can see that the model has a biased southerly shift in the jet stream, and it does not extend far enough into Europe. This is the case for both February and August (Fig. 2) and for all other months as well (Fig. S1). Difference maps between model and reanalysis therefore show a dipole pattern with negative differences to the north and over Europe and positive differences to the south of the jet stream in all months. However, we should keep in mind that the PI of the model represents preindustrial $CO_2$ concentrations, while ERAInt present-day values and therefore the actual bias should be smaller than seen in these figures. Indeed, there are several studies that have documented a poleward shift of the North Atlantic jet stream in reanalysis data, giving an estimation of around 1° to the north (Archer and Caldeira 2008; Rikus 2018; Totz et al. 2018). Therefore, the bias in our model is reduced but remains significant, as it is of 5°–10° magnitude, depending on the month (larger in winter; see Fig. S1). This bias in the wind should be taken into consideration when analyzing the results, as it also affects the patterns of variability, or weather regimes, studied.

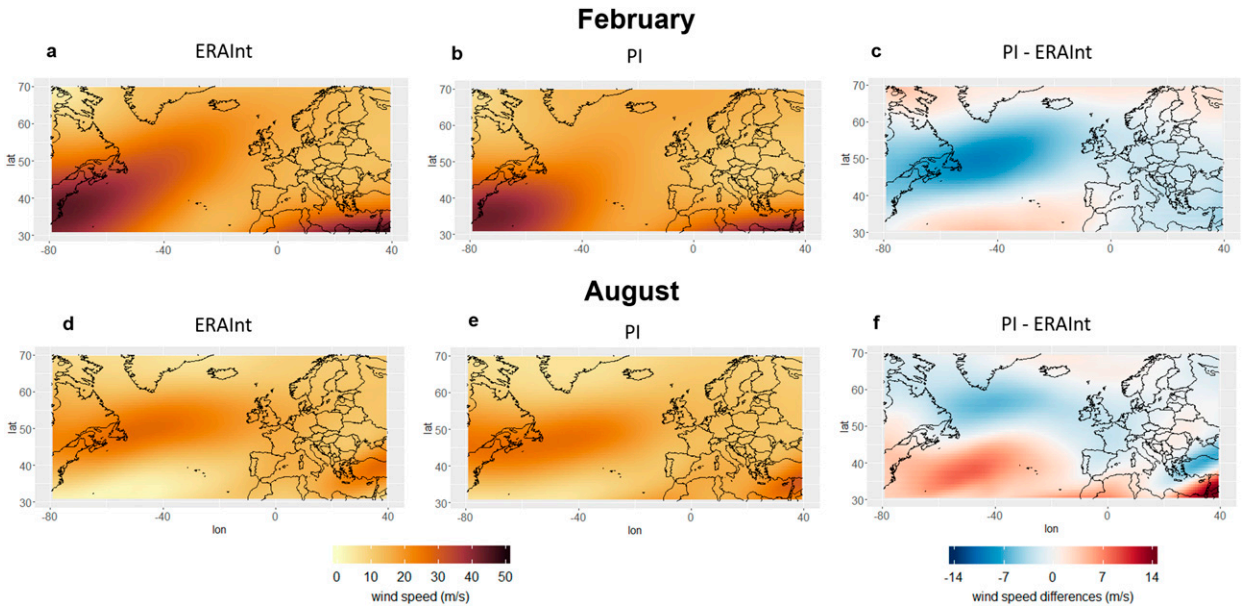


FIG. 2. Model validation of wind speed ($m\,s^{-1}$) at 250 hPa for (top) February and (bottom) August. Shown are (a),(d) the ERAInt climatology, (b),(e) the model PI climatology, and (c),(f) the differences of the two (PI − ERAInt).

Next, we analyze and compare the weather regimes extracted using SOMs for reanalysis and model data. The patterns obtained correspond to the four well-known Euro-Atlantic regimes described in various other studies [for a description and a visual depiction of those see, for example, Ferranti et al. (2015, their Fig. 1) and Fabiano et al. 2020]. However, one should keep in mind that we used streamfunction values at 250 hPa to define our weather regimes with the SOM method, instead of the more commonly used combination of geopotential height at 500 hPa and *k*-means (Madonna et al. 2017; Matsueda and Palmer 2018; Strommen et al. 2019). Thus, it is expected that the weather regimes we present here and their frequency of occurrence may not be exactly the same as in other studies, as these choices affect the results.

The results for the month of February are presented in Fig. 3 (see Figs. S2–S11 in the online supplemental material for all months). The model's SOMs bear good similarity to those of the reanalysis data, but the skill depends on the weather pattern. In general, streamfunction anomalies are less pronounced in the model, while the SOM patterns and frequencies are similar between the two. In particular, SOM1 shows the Scandinavian blocking (ScBl) regime, with a pronounced anticyclone over Scandinavia, which is captured by the model rather well, with a spatial correlation of 0.7. In SOM2 we see the Atlantic Ridge (AR), with a rather good representation (spatial correlation of 0.7), but shifted southward in the model. SOM3 represents a zonal circulation, or a positive NAO (Zo/NAO+), which is the least well represented in the model, with a spatial correlation of 0.4 and a southward bias as well. This southward displacement of the weather regimes seen in SOMs 2 and 3 is probably the reflection of the southward bias in the mean wind speed (Fig. 2c). Last, SOM4 shows the Greenland anticyclone, or the negative phase of the NAO (GA/NAO−), with a very good counterpart in the model, indicated by a high spatial correlation of 0.9. Additionally, in order to evaluate the ability of the model to reproduce the clusters seen in the reanalysis, we calculated the variance ratio (see text in the online supplementary material and Fig. S12) for both, following Fabiano et al. (2020), and we reached similar conclusions; the clusters of the model are less robust than the ones in the reanalysis data. However, the particularly high resolution of the model used here improves the results considerably with regard to lower-resolution models used in Fabiano et al. (2020).

For August (Fig. 4), and generally for summer months, the pattern correlations are lower compared to winter, probably because circulation in summer seems to be less regime-like and rather more continuous in phase space. In addition, there is a southward shift of the circulation patterns in the model, as in the mean wind (Fig. 2f), which degrades the spatial correlation values. Nevertheless, some of the summer weather patterns are still well captured by the model. For instance, SOM3 (Fig. 4), showing the Zo/NAO+ regime has a particularly good counterpart in the model with a 0.9 spatial correlation, although its frequency is overestimated. SOM1 is more zonal in ERAInt, while in the model it looks more like ScBl, with a center of positive streamfunction anomalies over Scandinavia. We should point out, though, that both SOM1 in the model and SOM2 in ERAInt represent atmospheric states that lie between two weather regimes, namely the ScBl and the AR, and cannot be clearly assigned to one of them. In SOM4 GA/NAO− is seen and the model performance is better again, with a spatial correlation of 0.6.

### b. *Changes in atmospheric circulation patterns under 2 × $CO_2$ and their impacts*

Next we analyze the differences in atmospheric circulation under increasing $CO_2$ concentrations. First of all, the response to this increase is characterized by a poleward and easterly shift of the jet stream in all months (Figs. 5e and 6e for February and

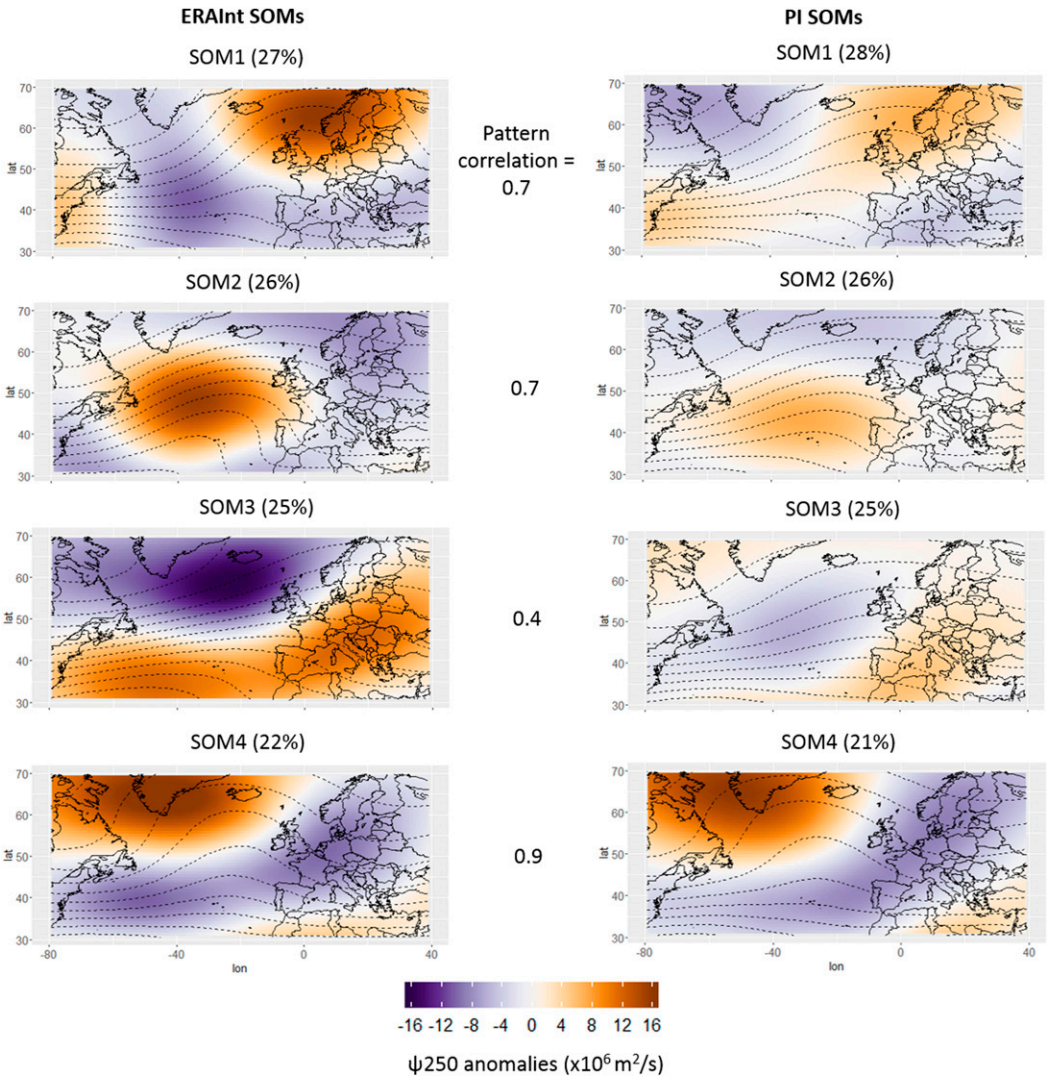


FIG. 3. Model validation for February SOM patterns. Mean streamfunction at 250 hPa ($\psi$250; dashed contour lines plotted every $10^7\,m^2\,s^{-1}$) and its anomaly from PI climatology (shading; all values are $\times 10^6\,m^2\,s^{-1}$). The domain mean has been removed from each pattern. ERAInt SOMs are shown in the left column and PI SOMs in the right. The frequency of each SOM ($f$) is shown in parentheses on top of each map and pattern correlations between SOM couples in the middle column.

August respectively), which is in agreement with several model studies (see, e.g., Barnes and Polvani 2013; Delcambre et al. 2013; Gonzalez et al. 2019).

Figure 5 presents the differences in PI and 2 × $CO_2$ projected SOM states for the month of February (results for all other months are presented in the online supplementary material; see Figs. S13–S22). The SOM spatial patterns shown in Figs. 5a–d represent the mean of all 10000 sets for each of the four projected 2 × $CO_2$_SOMs with their frequency of occurrence $f$ in parentheses, as well as the relative percentage change (RPC) in mean frequency compared to the projected PI_SOMs. SOM3, representing the Zo/NAO+ regime, increases substantially in occurrence frequency under 2 × $CO_2$ (RPC = 30% with 95% confidence interval of ±6.5%) and it becomes the dominant pattern ($f$ = 28%). Figure 5f presents boxplots for each SOM and shows that the full distribution of SOM3 shifts to higher values. SOM1, on the other hand, shows a significant decrease in frequency (RPC = −26%; 95% interval of ±5%), which is also evident in a shift of the full distributions shown in the boxplots. This is a pattern characterized by a ridge of positive streamfunction anomalies over Scandinavia and the United Kingdom, resembling the ScBl regime. SOM2, with similarities to AR, shows a minor increase with RPC of +8%, but the distribution of its frequencies becomes much broader, indicating larger variability. SOM4, a pronounced GA/NAO− pattern, is essentially unchanged as compared to PI (RPC = −2%). Additionally, Figs. 5g–j show the cumulative distributions (ECDFs) of Euclidean distances of all the

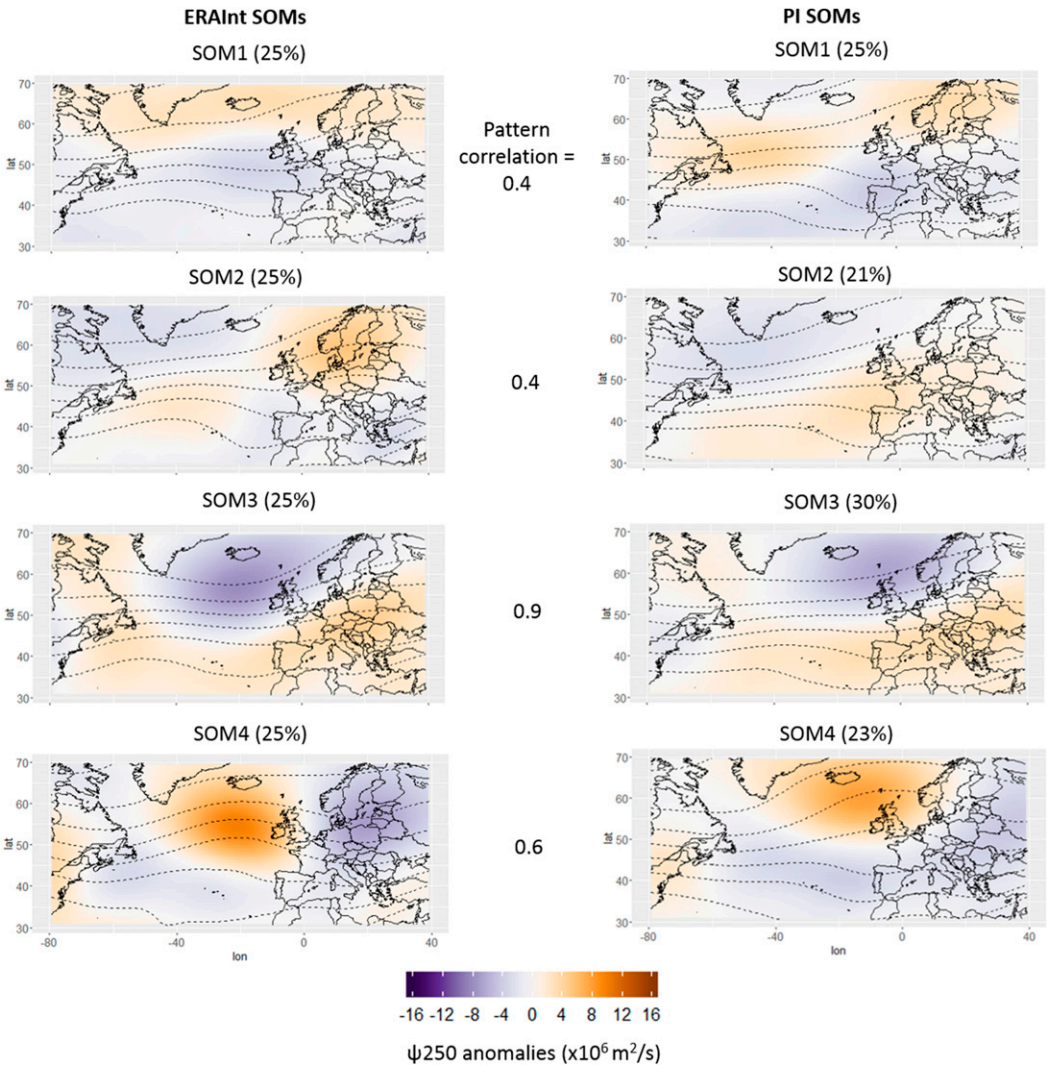


FIG. 4. As in Fig. 3, but for August SOM patterns.

5-day means assigned to each of the four SOMs, for both PI and $2 \times CO_2$. In all cases the distribution of distances for the $2 \times CO_2$ is shifted to higher values compared to PI. However, according to the Kolmogorov–Smirnoff test (ks), the ECDFs of the PI and $2 \times CO_2$ do not differ significantly for any of the SOMs (the ks statistic is plotted on the graphs and it shows the maximum absolute distance between a pair of ECDFs, while its critical value for statistical significance at $a = 0.05$ for this amount of data points and respective degrees of freedom is around 0.2). Additionally, we see that in every SOM there are a few units (red colored dots in the ECDF graphs of Figs. 5g–j) that exceed the outer boundary of each SOM, as indicated by the maximum Euclidean distance (vertical dashed line in the ECDF graphs of Figs. 5g–j) of the projected PI SOMs from the respective PI SOM centroids. We consider those units as newly emerging patterns in the $2 \times CO_2$ as they cannot be assigned to the original PI clusters. The frequency of occurrence of the emerging patterns is low (ranging from 0% to 2.1% in February) with maximum values in high winter and high summer months (see Fig. S23). Finally, it is worth mentioning that the increase in Zo/NAO+ weather pattern seen in February is a feature seen in other months as well, especially during the cold season (November–March; see respective figures in the supplementary material), with a mean increase (RPC) of around 20%, but also in July and September (Figs. S19 and S20). Moreover, ScBl is decreasing significantly in frequency in all months from December to April, with a mean RPC of 20% (Figs. S13–S16).

In Fig. 6 the results for August are presented. From the cumulative distributions of the Euclidean distances for August (Figs. 6g–j) we see that the clusters are more uniform than in winter, as they have smaller intracluster distances among input data and SOM centroids. Also, the distributions are more similar between PI and $2 \times CO_2$, showing that the differences in summer patterns are subtler compared to winter (Fig. 6f). The most frequent pattern in $2 \times CO_2$ in August is SOM2, with

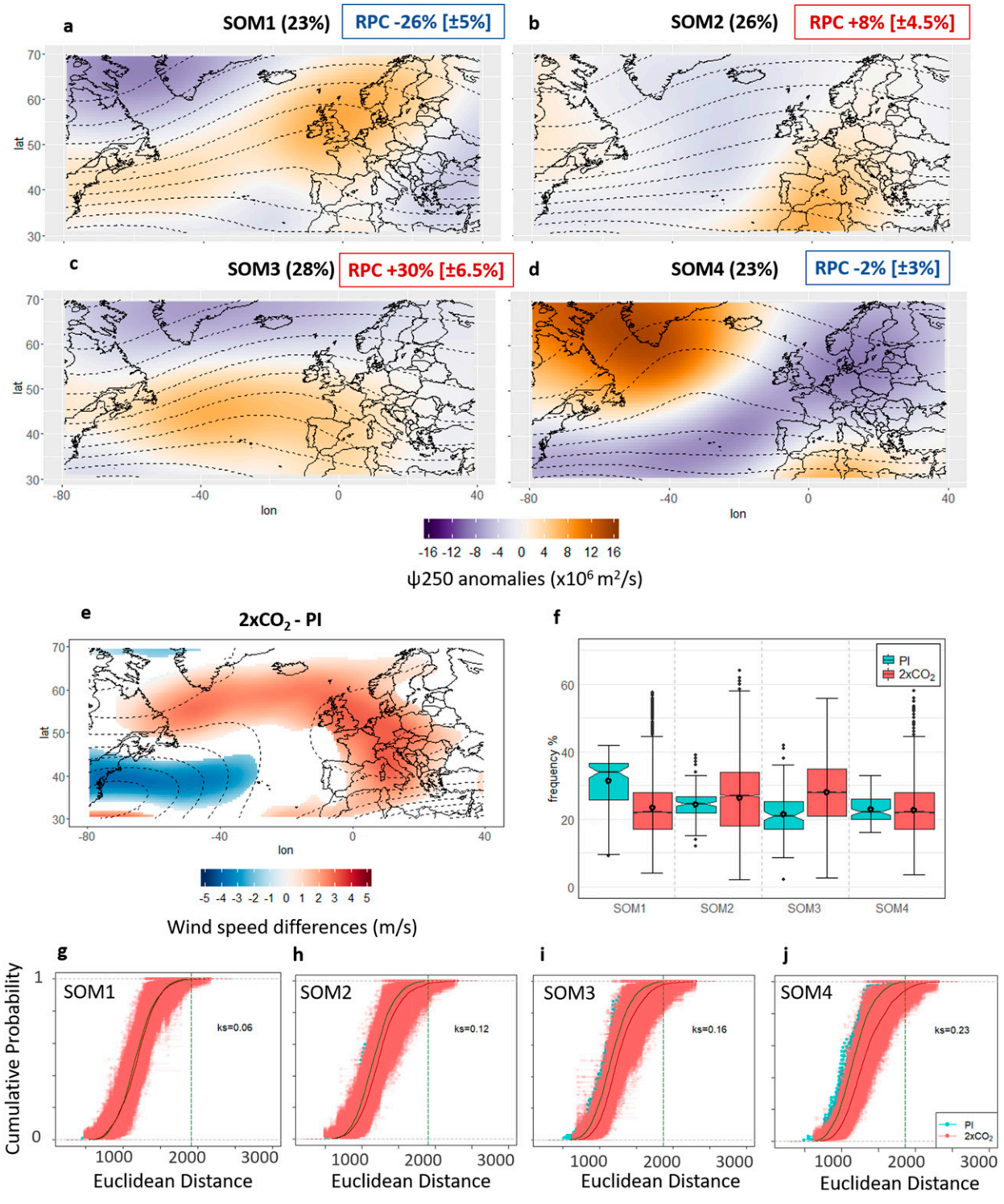


FIG. 5. Changes in atmospheric circulation patterns under 2 × $CO_2$ for February. (a)–(d) Mean streamfunction at 250 hPa ($\psi$250; contours plotted every $10^7$ $m^2$ $s^{-1}$) and its anomaly from PI climatology (shading; all values are $\times 10^6$ $m^2$ $s^{-1}$) for the four SOMs. The domain mean has been subtracted. The mean frequency of each projected 2 × $CO_2$_SOM ($f$) is shown in parentheses and next to it in a red (for increase) or blue (for decrease) box, the relative percentage change (RPC) in frequency compared to the projected PI_SOM mean with the 95% confidence interval in brackets. (e) Differences in the climatology of the mean wind field at 250 hPa between 2 × $CO_2$ and PI. Only statistically significant values ($p < 0.05$) are shown (shading). Dashed contour lines show the PI wind speed (plotted every 5 m $s^{-1}$). (f) Boxplots of frequency distributions of the four SOMs for projected PI_SOMs (green) and the projected 2 × $CO_2$ (red). The boxes contain the interquartile range (IQR: from the 25th percentile at the lower edge of the box to the

$f = 36\%$ and a pronounced relative change compared to the PI (RPC = +62%, 95% interval ±5%). This pattern is AR-like, with a center of positive anomalies over the northeast Atlantic, off the U.K. coast. This weather regime is increasing in frequency in almost all warm season months (May–August, Figs. S17–S19) and also in January–March (Figs. S14 and S15). It is thus a robust circulation change, especially across the warm season. All other SOMs present decreased frequencies in August. SOM1, a representation of ScBl, shows an RPC of −27%. SOM3 and SOM4, which are Zo/NAO+ and a GA/NAO+ like regimes, decrease by an RPC of −12% and −15%, respectively. When considering these results, one should definitely keep in mind that the summer weather regimes are not represented exceptionally well by the model; however, when checking the robustness of the documented changes in different SOM sizes and time aggregations (not shown) we do find similar indications.

The pronounced increase in zonal regimes, especially during winter, could favor excess precipitation amounts, and hence increase flood risk, over western Europe. To test this, we looked at how the changes in the frequency of this pattern affect precipitation (Fig. 7). Indeed, increased precipitation is expected over northwestern Europe, and especially over northern United Kingdom and the southwestern coast of Norway. The separation of thermodynamical (Fig. 7b) and dynamical effects (Fig. 7c) shows that they both act in the same direction, increasing precipitation over this region. The thermodynamical effect of being in a warmer climate has the largest contribution to this change (~75%), and the dynamical component further increases this trend (by ~25%). Indeed, the PDF of mean precipitation for this particular weather regime in the $2 \times CO_2$ run for northwestern Europe (region shown in the red box of Figs. 7b and 7c) is significantly shifted to larger values compared to the PI PDF (Fig. 7d).

On the other hand, the increased frequency of occurrence of the AR, which seems to dominate warm season months, is likely to favor summer droughts in Europe. Figure 8 shows the differences in precipitation due to the thermodynamical (Fig. 8b) and the dynamical (Fig. 8c) components. The effect of the thermodynamical component is more prominent (~60%) and it consists of less precipitation over west and central Europe and more precipitation over northeast and southeast Europe. The effect of the dynamical change (~40%) is consistent with that, further decreasing the precipitation amounts and enhancing the drying of western and central Europe. To get a better depiction of summer drought we looked at dry spells, defined by continuous days with precipitation below 1 mm and the differences between $2 \times CO_2$ and PI (Fig. 8d). Dry spells are seen to increase in length in western, central, and southern Europe by up to 8 days in August, while they show a decrease in northeastern Europe. Figure 8e shows the PDFs of dry spell length for PI and $2 \times CO_2$ for western and central Europe (region shown in the red box of Fig. 8d) and confirms this increased probability of occurrence of particularly long dry spells under increasing $CO_2$. Dry spells longer than 15 days were practically absent in the PI run.

## 4. Discussion

In this work, we looked at differences in upper-atmospheric circulation patterns between a preindustrial and a $2 \times CO_2$ model experiment. We defined clusters of circulation patterns with SOMs. To account for uncertainty in the model SOMs due to multidecadal variability and due to SOM initialization, we used random subsamples of the model runs and multiple randomly initialized SOMs and then projected the remaining PI, as well as $2 \times CO_2$ years, on those. This way we achieved an objective classification of atmospheric circulation patterns and we got an estimation of the uncertainties of both the method and the internal variability of the data.

Although we used a very high-resolution coupled climate model, the comparison to reanalysis data revealed biases in the simulation of the mean state of wind magnitude over North Atlantic, which is also reflected in the representation of the atmospheric circulation patterns. Handorf and Dethloff (2012) found that the skill of models in simulating spatial teleconnection patterns in the Northern Hemisphere largely depends on the quality of the simulated zonal wind variability. Indeed, many models show a too-zonal, southerly shifted North Atlantic jet, especially in winter (Woollings 2010; Chang et al. 2012; Zappa et al. 2013). Nonetheless, we should account for the fact that the preindustrial run of the model has lower $CO_2$ concentrations than the ERAInt dataset and thus the actual bias is somewhat reduced. However, to analyze further the sources of biases in the model is beyond the scope of the present study. Regarding the representation of circulation patterns in the model, we find that best (worst) results are obtained for winter (summer) months, which may have to do with the fact that the number of clusters used is more optimal for winter (Cortesi et al. 2019) whereas summer circulation is less regime-like.

We find significant changes in the frequency of circulation patterns in a $2 \times CO_2$ climate both for the cold and warm season. This fact, in combination with the low occurrence of emerging patterns in the $2 \times CO_2$, seems to confirm the hypothesis of Palmer (1999) that the response of the climate system to anthropogenic climate change is mainly manifested in terms of changes to the frequency of natural modes of

←

75th percentile at the upper edge of the box) of the values, while the whiskers extend to 1.5 × IQR and the black dots beyond them are the outliers. The median is represented by the horizontal line and notches around it show its 5th and 95th percentile. Mean frequency is shown with open circle. (g)–(j) Empirical cumulative distribution functions of the Euclidean distances for the units assigned to each of the four SOMs from the respective PI_SOM centroid for projected PI_SOMs (green) and projected $2 \times CO_2$ (red). Respective colored lines show the mean ECDF. Vertical dashed lines show the maximum Euclidean distance for projected PI_SOMs. The Kolmogorov–Smirnoff statistic (ks) is plotted on each of the ECDF graphs.

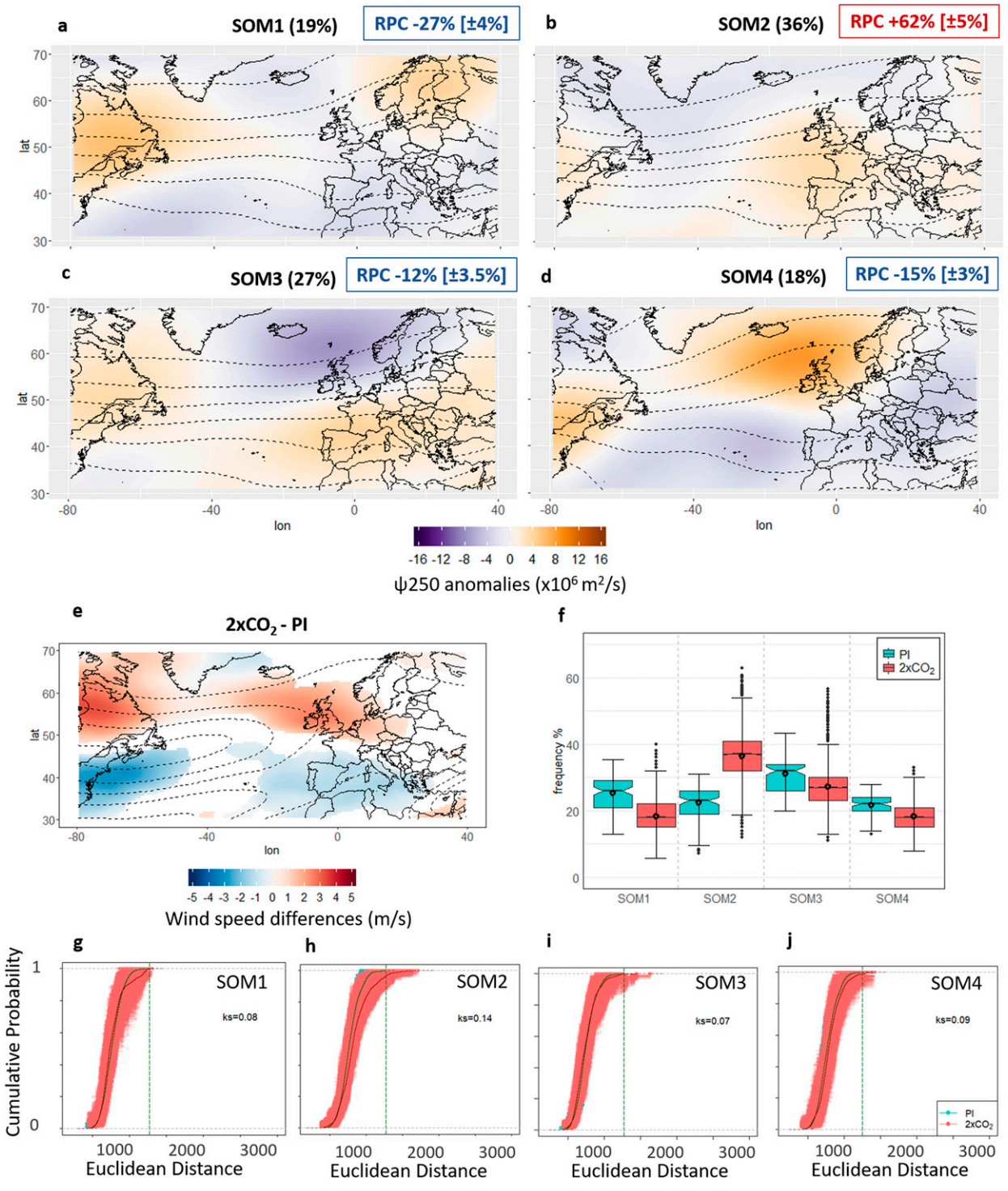


FIG. 6. As in Fig. 5, but for August.

variability and not with the emergence of new regime patterns themselves. In February, and to a certain degree in the whole cold season (November–March), we find a robust increase in the frequency of zonal flow regimes, corresponding to different flavors of the positive NAO phase (Rousi et al. 2020). This pattern increases significantly in all months from November to March, and also in September, May, and July. On average, for the cold season, this zonal regime will occur around 20% more

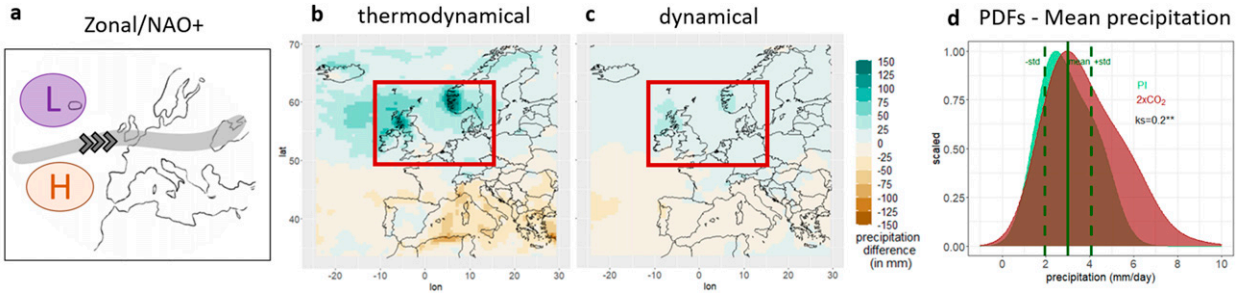


FIG. 7. Impacts of increasing zonal/NAO+ regime (SOM3 as seen in Fig. 5c) on precipitation in February. (a) Schematic representation of the zonal/NAO+ regime with a pronounced low pressure system over Iceland and a pronounced high pressure system over the Azores. The jet stream is depicted with gray shading. (b) Differences in total precipitation amount (mm) for the zonal/NAO+ regime between $2 \times CO_2$ and PI over Europe: thermodynamical component. (c) As in (b), but for the dynamical component. (d) PDFs of mean precipitation for PI (green) and $2 \times CO_2$ (red) for the zonal/NAO+ regime for northwestern Europe [region in the red box of (b) and (c)] and the ks distance statistic of the two distributions [two asterisks (**) denote statistical significance at $p < 0.1$]. Mean (green vertical line) and standard deviation (green dashed vertical lines) of the PI distribution are shown.

often compared to the preindustrial climate. An increase in NAO+ has been found in CMIP5 models by Gillett and Fyfe (2013) in all seasons and especially in autumn. Recently, Fabiano et al. (2021) documented an increase in the NAO+ frequency and persistence during the second half of the twenty-first century in all CMIP6 models and scenarios, which they find consistent with a squeezing of the jet around its central position (Peings et al. 2018; Oudar et al. 2020) and with reduced variability of the jet (Barnes and Polvani 2013). However, given the strongly negative NAO index during the 2009/10 and 2010/11 boreal winters, some studies suggest that the reduced sea ice extent over the Arctic may exert an influence toward more NAO− events (Jaiser et al. 2012). In our results, NAO− was found to significantly increase only in the month of April (Fig. S15), while significantly decreasing in 7 months.

The increase in the zonal flow regime seems to reflect the shift in the mean state, which also becomes more zonal and shifts eastward under increasing $CO_2$. This is in agreement with the findings of Lau and Ploshay (2013) showing a similar response pattern in sea level pressure over the North Atlantic sector. The physical processes responsible for these changes are related to changes in the tropospheric thermal structure. The relative strength of the upper tropospheric subtropical enhanced warming and the surface midlatitude reduced warming modifies the meridional temperature strength and affects the zonal wind structure according to the thermal wind relationship (Haarsma et al. 2013). Additionally, changes in the AMOC significantly affect the SST distribution in the Atlantic and consequently the zonal wind in a warming climate. Woollings et al. (2012) showed that the strengthening and eastward extension of the North Atlantic storm track is related to the weakening of the AMOC. This is also supported by Lau and Ploshay (2013), who found that an enhanced meridional SST gradient over the northwestern Atlantic due to the cooling trend in the region is accompanied by strengthened baroclinicity in the lower troposphere and enhanced storm track activity toward northwestern Europe.

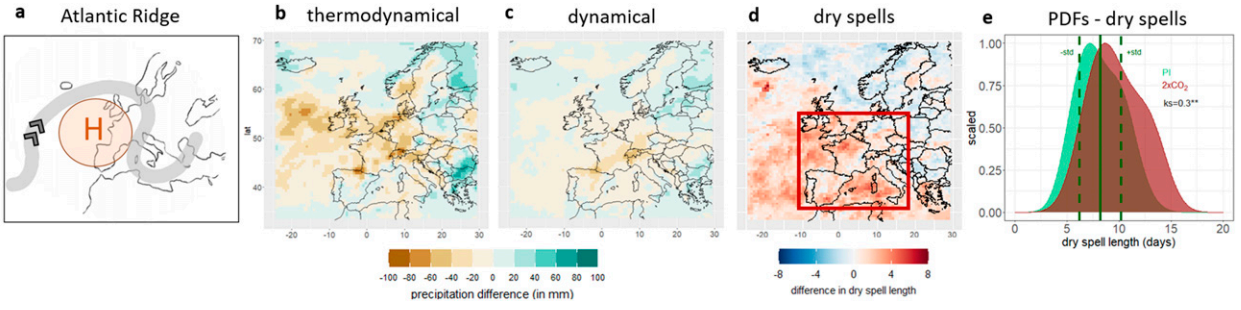


FIG. 8. Impacts of increasing Atlantic Ridge regime (SOM2 as seen in Fig. 6b) on precipitation and dry spells in August. (a) Schematic representation of the Atlantic Ridge regime with an extended blocking high pressure system over northeastern Atlantic/western Europe. The jet stream is depicted with gray shading. (b) Differences in total precipitation amount (mm) for the AR regime between $2 \times CO_2$ and PI over Europe: thermodynamical component. (c) As in (b), but for the dynamical component. (d) Differences in dry spell length (in days) for the AR regime between $2 \times CO_2$ and PI over Europe. (e) PDFs of dry spell length for PI (green) and $2 \times CO_2$ (red) for the AR regime for western/central Europe (region in the red box of panel d) and the ks distance statistic of the two distributions [two asterisks (**) denote statistical significance at $p < 0.1$]. Mean (green vertical line) and standard deviation (green dashed vertical lines) of the PI distribution are shown.

An increase in strong zonal flow regimes over the Atlantic presents an increased flood risk as such regimes are connected to warmer than normal temperatures, stormier weather, and heavy rainfall over northwestern Europe and the United Kingdom in particular. The winter of 2013/14 for example, was extreme in terms of rainfall amounts and prolonged flooding in the United Kingdom as a result of this type of circulation (Knight et al. 2017). According to Christidis and Stott (2015b) it is reasonable to assume that climate change has increased the risk of such extremes by increasing the frequency of the relevant atmospheric circulation patterns. Indeed, Vautard et al. (2016) attribute the excess rainfall of that winter to human-induced changes, of both thermodynamical and dynamical nature. They find that the zonal regime, which is the wettest, increases in frequency when comparing a factual (with greenhouse gas and aerosol concentrations as observed today) to a counterfactual (with the anthropogenic forcing removed) world, while the amount of precipitation it brings is also larger for events of the same return period. In general, a more zonal North Atlantic jet stream in winter has high-impact implications on flood risk and economic loss, wave activity, and coastal soil erosion (Castelle et al. 2017), wind and solar energy potential (van der Wiel et al. 2019), and others. While uncertainty remains with respect to future circulation changes (Shepherd 2014), this strong zonal flow regime now emerges as a robust feature based on a range of studies that use different climate models, circulation metrics and observational analyses (van Ulden and van Oldenborgh 2006; Schaller et al. 2016). We showed that the 30% increase in relative occurrence-frequency of this regime in February, as reported here, will result in excess rainfall over northwestern Europe, acting on top of the thermodynamically induced increase of rainfall in the region. Therefore, this increase, combined with the enhanced water-holding capacity of warmer air and long-term sea level rise, presents enhanced compound flood risks for the United Kingdom, the Netherlands, and other northwestern European countries (Ward et al. 2018).

In August (and also in the extended warm season May–August), we see a substantial increase by ~60% (~40%) of the Atlantic Ridge regime, which corresponds to increased pressure directly off the coast of the United Kingdom. Again, this emerges as a robust finding consistent with previous studies regarding changes in summer circulation over the North Atlantic. The higher pressures over the British Isles enhance easterly winds and amplify continental warming and drying of western Europe (Haarsma et al. 2009). Indeed, we could show that under increased occurrence of this weather regime in a warming world, precipitation amounts will be smaller and dry spells will become longer in western and central Europe. Lau and Ploshay (2013) found that in summer the projected enhancement of convection over the eastern tropical Pacific is accompanied by a wave train toward North America, the North Atlantic, and Europe, associated with weakened storm track activity at 40°–50°N and an eddy forcing pattern similar to the summertime SLP response in the late twenty-first century. This region of increased pressure is evident in the upper atmosphere in our results for all warm season months. Our results are also consistent with the findings by Lehmann et al. (2014) who show that under global warming the CMIP5 model ensemble shows substantial decrease in storm track activity during boreal summer.

Like for winter, changes in oceanic currents seem to play a significant role in this change during summer as well. The slowdown of the AMOC causes a reduction in the associated northward heat transport and a cooling of the North Atlantic (Caesar et al. 2018) that may trigger extreme heatwaves over central Europe (Duchez et al. 2016). By performing idealized model experiments, Haarsma et al. (2015) showed that the decline of the AMOC is the primary cause of the anomalous high pressure system west of the United Kingdom. Our results seem to confirm these findings as the AMOC decline in the $2 \times CO_2$ run of the CM2.6 model may well be one of the drivers of the increased frequency of high-pressure systems over northeastern Atlantic in summer. This kind of weather pattern configuration can result from a circumglobal Rossby wave pattern characterized by a strongly meandering jet stream, such as in many recent summers with simultaneous extremes over the Northern Hemisphere midlatitudes, like those of 2010 and 2018 (Kornhuber et al. 2019, 2020). The ~40% increase, which reaches ~60% in August, in high pressure regimes over the United Kingdom, as reported here, poses substantial drought risks for Europe. The resulting easterly continental flow that brings dry air, in combination with the more rapid drying of soils when the overlying atmosphere is warmer, similar to the situation in 2018, imposes high-end risks for society, including extreme heat waves, wildfires, and harvest failures.

Further we see, across all months and seasons, a decrease in frequency of the Scandinavian blocking under increasing $CO_2$. Such a decrease could have some positive implications, as such a configuration of the circulation is often associated with regional extreme weather, from heatwaves in summer to severe cold in winter across western Europe and central Russia (Woollings et al. 2018). A decrease in Scandinavian blocking would also be positive for wind production and energy demand, as during this regime there is low production combined with high demand (van der Wiel et al. 2019). Projections of the response of Euro-Atlantic blocking to increasing greenhouse gases indicate a reduced frequency in both winter and summer (Matsueda et al. 2009; Masato et al. 2013; Davini and D'Andrea 2020). It is important, though, to keep in mind that climate models exhibit significant blocking biases (Scaife et al. 2010; Davini and D'Andrea 2016), although different studies show that improvements may be made with increasing model resolution (Anstey et al. 2013).

This study is based on one high-resolution GCM, which was chosen because it provides the highest global resolution over the ocean and thus a very realistic representation of the AMOC and of mesoscale ocean eddies, which in turn affect the overlying atmospheric circulation. Clearly, this is an important advantage (Haarsma et al. 2015); however, it would be useful to test the sensitivity of our findings in different models, such as the CMIP6 ones, that according to Fabiano et al. (2021) have improved compared to the CMIP5 models in representing weather regimes, of different resolution and complexity and in different ensembles. The methodology used here calls for further developments, for instance the use of weather regimes

to study circulation changes has some important advantages but at the same time several limitations, especially for summer. Further impact analyses, such as of extreme events, may shed more light on the role of thermodynamical and dynamical changes on different variables.

## 5. Conclusions

The main conclusions of the study can be summarized in the following points. With the use of CM2.6, a high-resolution coupled global climate model, and an objective clustering method, we assessed changes in North Atlantic atmospheric circulation patterns under increasing $CO_2$ concentrations. We found significant differences in frequency of occurrence of certain patterns in all months. Those differences are robust, and they stand out from the uncertainty and the internal variability of the model. In February we see a substantial increase (with a relative change ranging from +24% to +36%) of zonal circulation regimes over the North Atlantic and western Europe, which leads to increased precipitation over northwestern Europe posing high flood risk for these areas. In August the most robust change (ranging from +57% to +67%) is that of increased high pressure systems off the U.K. coast. This circulation change results in less precipitation and longer dry spells over large parts of western and central Europe, enhancing drought risk in summer.

*Acknowledgments.* We thank NOAA/GFDL for running the GFDL-CM2.6 model and Dr. Stephen Griffies of GFDL for kindly providing us with the CM2.6 model data. We also thank the European Centre for Medium-Range Weather Forecasts (ECMWF) for making the ERA-Interim reanalysis dataset available. We are grateful to three anonymous reviewers, who gave thoughtful suggestions and helped improve the original manuscript. ER and DC were supported by the German Federal Ministry of Education and Research within the GOTHAM project (Grant 01LP1611A). The authors declare that there is no conflict of interest.

*Data availability statement.* The CM2.6 model output used for this study is available from E. Rousi (rousi@pik-potsdam.de) upon reasonable request. ERA-Interim datasets are publicly available by the European Centre for Medium-Range Weather Forecasts (ECMWF).

## REFERENCES

Alexander, L. V., P. Uotila, N. Nicholls, and A. Lynch, 2010: A new daily pressure dataset for Australia and its application to the assessment of changes in synoptic patterns during the last century. *J. Climate*, **23**, 1111–1126, https://doi.org/10.1175/2009JCLI2972.1.

Allan, D., and R. P. Allan, 2019: Seasonal changes in the North Atlantic cold anomaly: The influence of cold surface waters from coastal Greenland and warming trends associated with variations in subarctic sea ice cover. *J. Geophys. Res. Oceans*, **124**, 9040–9052, https://doi.org/10.1029/2019JC015379.

Anstey, J. A., and Coauthors, 2013: Multi-model analysis of Northern Hemisphere winter blocking: Model biases and the role of resolution. *J. Geophys. Res. Atmos.*, **118**, 3956–3971, https://doi.org/10.1002/jgrd.50231.

Archer, C. L., and K. Caldeira, 2008: Historical trends in the jet streams. *Geophys. Res. Lett.*, **35**, L08803, https://doi.org/10.1029/2008GL033614.

Barker, L., J. Hannaford, K. Muchan, S. Turner, and S. Parry, 2016: The winter 2015/2016 floods in the UK: A hydrological appraisal. *Weather*, **71**, 324–333, https://doi.org/10.1002/wea.2822.

Barnes, E. A., and L. Polvani, 2013: Response of the midlatitude jets, and of their variability, to increased greenhouse gases in the CMIP5 models. *J. Climate*, **26**, 7117–7135, https://doi.org/10.1175/JCLI-D-12-00536.1.

Blöschl, G., and Coauthors, 2019: Changing climate both increases and decreases European river floods. *Nature*, **573**, 108–111, https://doi.org/10.1038/s41586-019-1495-6.

Branstator, G., 2002: Circumglobal teleconnections, the jet stream waveguide, and the North Atlantic Oscillation. *J. Climate*, **15**, 1893–1910, https://doi.org/10.1175/1520-0442(2002)015<1893:CTTJSW>2.0.CO;2.

——, and F. Selten, 2009: "Mode of variability" and climate change. *J. Climate*, **22**, 2639–2658, https://doi.org/10.1175/2008JCLI2517.1.

Caesar, A. L., S. Rahmstorf, A. Robinson, G. Feulner, and V. Saba, 2018: Observed fingerprint of a weakening Atlantic Ocean overturning circulation. *Nature*, **556**, 191–196, https://doi.org/10.1038/s41586-018-0006-5.

Cassou, C., L. Terray, J. W. Hurrell, and C. Deser, 2004: North Atlantic winter climate regimes: Spatial asymmetry, stationarity with time, and oceanic forcing. *J. Climate*, **17**, 1055–1068, https://doi.org/10.1175/1520-0442(2004)017<1055:NAWCRS>2.0.CO;2.

Castelle, B., G. Dodet, G. Masselink, and T. Scott, 2017: A new climate index controlling winter wave activity along the Atlantic coast of Europe: The West Europe pressure anomaly. *Geophys. Res. Lett.*, **44**, 1384–1392, https://doi.org/10.1002/2016GL072379.

Chang, C. H., and N. C. Johnson, 2015: The continuum of wintertime Southern Hemisphere atmospheric teleconnection patterns. *J. Climate*, **28**, 9507–9529, https://doi.org/10.1175/JCLI-D-14-00739.1.

Chang, E. K. M., Y. Guo, and X. Xia, 2012: CMIP5 multimodel ensemble projection of storm track change under global warming. *J. Geophys. Res.*, **117**, D23118, https://doi.org/10.1029/2012JD018578.

——, C. Ma, C. Zheng, and A. M. W. Yau, 2016: Observed and projected decrease in Northern Hemisphere extratropical cyclone activity in summer and its impacts on maximum temperature. *Geophys. Res. Lett.*, **43**, 2200–2208, https://doi.org/10.1002/2016GL068172.

Chemke, R., L. Zanna, and L. M. Polvani, 2020: Identifying a human signal in the North Atlantic warming hole. *Nat. Commun.*, **11**, 1540, https://doi.org/10.1038/s41467-020-15285-x.

Christidis, N., and P. A. Stott, 2015a: Extreme rainfall in the United Kingdom during winter 2013/14: The role of atmospheric circulation and climate change. *Bull. Amer. Meteor. Soc.*, **96**, S46–S50, https://doi.org/10.1175/BAMS-D-15-00094.1.

——, and ——, 2015b: Changes in the geopotential height at 500 hPa under the influence of external climatic forcings. *Geophys. Res. Lett.*, **42**, 10 798–10 806, https://doi.org/10.1002/2015GL066669.

——, G. S. Jones, and P. A. Stott, 2015: Dramatically increasing chance of extremely hot summers since the 2003 European heatwave. *Nat. Climate Change*, **5**, 46–50, https://doi.org/10.1038/nclimate2468.

Cortesi, N., V. Torralba, N. González-Reviriego, A. Soret, and F. J. Doblas-Reyes, 2019: Characterization of European wind speed variability using weather regimes. *Climate Dyn.*, **53**, 4961–4976, https://doi.org/10.1007/s00382-019-04839-5.

Coumou, D., and S. Rahmstorf, 2012: A decade of weather extremes. *Nat. Climate Change*, **2**, 491–496, https://doi.org/10.1038/nclimate1452.

——, J. Lehmann, and J. Beckmann, 2015: The weakening summer circulation in the Northern Hemisphere mid-latitudes. *Science*, **348**, 324–327, https://doi.org/10.1126/science.1261768.

——, G. Di Capua, S. Vavrus, L. Wang, and S. Wang, 2018: The influence of Arctic amplification on mid-latitude summer circulation. *Nat. Commun.*, **9**, 2959, https://doi.org/10.1038/s41467-018-05256-8.

Czaja, A., C. Frankignoul, S. Minobe, and B. Vannière, 2019: Simulating the midlatitude atmospheric circulation: What might we gain from high-resolution modeling of air–sea interactions? *Curr. Climate Change Rep.*, **5**, 390–406, https://doi.org/10.1007/s40641-019-00148-5.

Davini, P., and F. D'Andrea, 2016: Northern Hemisphere atmospheric blocking representation in global climate models: Twenty years of improvements? *J. Climate*, **29**, 8823–8840, https://doi.org/10.1175/JCLI-D-16-0242.1.

——, and ——, 2020: From CMIP3 to CMIP6: Northern Hemisphere atmospheric blocking simulation in present and future climate. *J. Climate*, **33**, 10 021–10 038, https://doi.org/10.1175/JCLI-D-19-0862.1.

Dawson, A., T. N. Palmer, and S. Corti, 2012: Simulating regime structures in weather and climate prediction models. *Geophys. Res. Lett.*, **39**, L21805, https://doi.org/10.1029/2012GL053284.

Dee, D. P., and Coauthors, 2011: The ERA-Interim reanalysis: Configuration and performance of the data assimilation system. *Quart. J. Roy. Meteor. Soc.*, **137**, 553–597, https://doi.org/10.1002/qj.828.

Delcambre, S. C., D. J. Lorenz, D. J. Vimont, and J. E. Martin, 2013: Diagnosing Northern Hemisphere jet portrayal in 17 CMIP3 global climate models: Twenty-first-century projections. *J. Climate*, **26**, 4930–4946, https://doi.org/10.1175/JCLI-D-12-00359.1.

Delworth, T. L., and Coauthors, 2012: Simulated climate and climate change in the GFDL CM2.5 high-resolution coupled climate model. *J. Climate*, **25**, 2755–2781, https://doi.org/10.1175/JCLI-D-11-00316.1.

Duchez, A., and Coauthors, 2016: Drivers of exceptionally cold North Atlantic Ocean temperatures and their link to the 2015 European heat wave. *Environ. Res. Lett.*, **11**, 074004, https://doi.org/10.1088/1748-9326/11/7/074004.

Fabiano, F., H. M. Christensen, K. Strommen, P. Athanasiadis, A. Baker, R. Schiemann, and S. Corti, 2020: Euro-Atlantic weather regimes in the PRIMAVERA coupled climate simulations: Impact of resolution and mean state biases on model performance. *Climate Dyn.*, **54**, 5031–5048, https://doi.org/10.1007/s00382-020-05271-w.

——, V. Meccia, P. Davini, P. Ghinassi, and S. Corti, 2021: A regime view of future atmospheric circulation changes in northern mid-latitudes. *Wea. Climate Dyn. Discuss.*, https://doi.org/10.5194/wcd-2020-37, in press.

Ferranti, L., S. Corti, and M. Janousek, 2015: Flow-dependent verification of the ECMWF ensemble over the Euro-Atlantic sector. *Quart. J. Roy. Meteor. Soc.*, **141**, 916–924, https://doi.org/10.1002/qj.2411.

Fort, J., P. Letremy, and M. Cottrell, 2002: Advantages and drawbacks of the Batch Kohonen algorithm. *Proc. European Symp. on Artificial Neural Networks (ESANN)*, Bruges, Belgium, 223–230.

Forzieri, G., and Coauthors, 2016: Multi-hazard assessment in Europe under climate change. *Climatic Change*, **137**, 105–119, https://doi.org/10.1007/s10584-016-1661-x.

Francis, J. A., N. Skific, and S. J. Vavrus, 2018: North American weather regimes are becoming more persistent: Is Arctic amplification a factor? *Geophys. Res. Lett.*, **45**, 11 414–11 422, https://doi.org/10.1029/2018GL080252.

Gervais, M., J. Shaman, and Y. Kushnir, 2020: Impact of the North Atlantic warming hole on sensible weather. *J. Climate*, **33**, 4255–4271, https://doi.org/10.1175/JCLI-D-19-0636.1.

Gillett, N. P., and J. C. Fyfe, 2013: Annular mode changes in the CMIP5 simulations. *Geophys. Res. Lett.*, **40**, 1189–1193, https://doi.org/10.1002/grl.50249.

Gonzalez, P. L. M., D. J. Brayshaw, and G. Zappa, 2019: The contribution of North Atlantic atmospheric circulation shifts to future wind speed projections for wind power over Europe. *Climate Dyn.*, **53**, 4095–4113, https://doi.org/10.1007/s00382-019-04776-3.

Griffies, S. M., and Coauthors, 2015: Impacts on ocean heat from transient mesoscale eddies in a hierarchy of climate models. *J. Climate*, **28**, 952–977, https://doi.org/10.1175/JCLI-D-14-00353.1.

Guèye, A. K., S. Janicot, A. Niang, S. Sawadogo, B. Sultan, A. Diongue-Niang, and S. Thiria, 2012: Weather regimes over Senegal during the summer monsoon season using self-organizing maps and hierarchical ascendant classification. Part II: Interannual time scale. *Climate Dyn.*, **39**, 2251–2272, https://doi.org/10.1007/s00382-012-1346-8.

Haarsma, R. J., F. Selten, B. van den Hurk, W. Hazeleger, and X. Wang, 2009: Drier Mediterranean soils due to greenhouse warming bring easterly winds over summertime central Europe. *Geophys. Res. Lett.*, **36**, L04705, https://doi.org/10.1029/2008GL036617.

——, ——, and G. J. van Oldenborgh, 2013: Anthropogenic changes of the thermal and zonal flow structure over western Europe and eastern North Atlantic in CMIP3 and CMIP5 models. *Climate Dyn.*, **41**, 2577–2588, https://doi.org/10.1007/s00382-013-1734-8.

——, F. M. Selten, and S. S. Drijfhout, 2015: Decelerating Atlantic meridional overturning circulation main cause of future west European summer atmospheric circulation changes. *Environ. Res. Lett.*, **10**, 094007, https://doi.org/10.1088/1748-9326/10/9/094007.

——, J. García-Serrano, C. Prodhomme, O. Bellprat, P. Davini, and S. Drijfhout, 2019: Sensitivity of winter North Atlantic–European climate to resolved atmosphere and ocean dynamics. *Sci. Rep.*, **9**, 13358, https://doi.org/10.1038/s41598-019-49865-9.

Handorf, D., and K. Dethloff, 2012: How well do state-of-the-art atmosphere–ocean general circulation models reproduce atmospheric teleconnection patterns? *Tellus*, **64A**, 19777, https://doi.org/10.3402/TELLUSA.V64i0.19777.

Hewitson, B. C., and R. G. Crane, 2002: Self-organizing maps: Application to synoptic climatology. *Climate Res.*, **22**, 13–26, https://doi.org/10.3354/cr022013.

Horton, D. E., N. Johnson, D. Singh, D. Swain, B. Rajaratnam, and N. Diffenbaugh, 2015: Contribution of changes in atmospheric circulation patterns to extreme temperature trends. *Nature*, **522**, 465–469, https://doi.org/10.1038/nature14550.

Huth, R., J. Kyselý, and L. Pokorná, 2000: A GCM simulation of heat waves, dry spells, and their relationships to circu-

lation. *Climatic Change*, **46**, 29–60, https://doi.org/10.1023/A:1005633925903.

IPCC, 2013: *Climate Change 2013: The Physical Science Basis*. Cambridge University Press, 1535 pp., https://doi.org/10.1017/CBO9781107415324.

Jaiser, R., K. Dethloff, D. Handorf, A. Rinke, and J. Cohen, 2012: Impact of sea ice cover changes on the Northern Hemisphere atmospheric winter circulation. *Tellus*, **64A**, 11595, https://doi.org/10.3402/tellusa.v64i0.11595.

Josey, S. A., J. J.-M. Hirschi, B. Sinha, A. Duchez, J. P. Grist, and R. Marsh, 2018: The recent Atlantic cold anomaly: Causes, consequences, and related phenomena. *Annu. Rev. Mar. Sci.*, **10**, 475–501, https://doi.org/10.1146/annurev-marine-121916-063102.

Keil, P., T. Mauritsen, J. Jungclaus, C. Hedemann, D. Olonscheck, and R. Ghosh, 2020: Multiple drivers of the North Atlantic warming hole. *Nat. Climate Change*, **10**, 667–671, https://doi.org/10.1038/s41558-020-0819-8.

Kimoto, M., and M. Ghil, 1993: Multiple flow regimes in the Northern Hemisphere winter. Part II: Sectorial regimes and preferred transitions. *J. Atmos. Sci.*, **50**, 2645–2673, https://doi.org/10.1175/1520-0469(1993)050<2645:MFRITN>2.0.CO;2.

Knight, J. R., and Coauthors, 2017: Global meteorological influences on the record UK rainfall of winter 2013-14. *Environ. Res. Lett.*, **12**, 074001, https://doi.org/10.1088/1748-9326/aa693c.

Kohonen, T., 2013: Essentials of the self-organizing map. *Neural Network*, **37**, 52–65, https://doi.org/10.1016/j.neunet.2012.09.018.

Kornhuber, K., S. Osprey, D. Coumou, S. Petri, V. Petoukhov, S. Rahmstorf, and L. Gray, 2019: Extreme weather events in early summer 2018 connected by a recurrent hemispheric wave-7 pattern. *Environ. Res. Lett.*, **14**, 054002, https://doi.org/10.1088/1748-9326/ab13bf.

——, D. Coumou, E. Vogel, C. Lesk, J. F. Donges, J. Lehmann, and R. M. Horton, 2020: Amplified Rossby waves enhance risk of concurrent heatwaves in major breadbasket regions. *Nat. Climate Change*, **10**, 48–53, https://doi.org/10.1038/s41558-019-0637-z.

Kretschmer, M., J. Runge, and D. Coumou, 2017: Early prediction of extreme stratospheric polar vortex states based on causal precursors. *Geophys. Res. Lett.*, **44**, 8592–8600, https://doi.org/10.1002/2017GL074696.

——, J. Cohen, V. Matthias, J. Runge, and D. Coumou, 2018: The different stratospheric influence on cold-extremes in Eurasia and North America. *npj Climate Atmos. Sci.*, **1**, 44, https://doi.org/10.1038/s41612-018-0054-4.

Latif, M., T. Park, and W. Park, 2019: Decadal Atlantic Meridional Overturning Circulation slowing events in a climate model. *Climate Dyn.*, **53**, 1111–1124, https://doi.org/10.1007/s00382-019-04772-7.

Lau, N. C., and J. J. Ploshay, 2013: Model projections of the changes in atmospheric circulation and surface climate over North America, the North Atlantic, and Europe in the twenty-first century. *J. Climate*, **26**, 9603–9620, https://doi.org/10.1175/JCLI-D-13-00151.1.

Lee, M. H., S. Lee, H. J. Song, and C. H. Ho, 2017: The recent increase in the occurrence of a boreal summer teleconnection and its relationship with temperature extremes. *J. Climate*, **30**, 7493–7504, https://doi.org/10.1175/JCLI-D-16-0094.1.

Lehmann, J., D. Coumou, K. Frieler, A. V. Eliseev, and A. Levermann, 2014: Future changes in extratropical storm tracks and baroclinicity under climate change. *Environ. Res. Lett.*, **9**, 084002, https://doi.org/10.1088/1748-9326/9/8/084002.

Luong, T. M., H. P. Dasari, and I. Hoteit, 2020: Extreme precipitation events are becoming less frequent but more intense over Jeddah, Saudi Arabia. Are shifting weather regimes the cause? *Atmos. Sci. Lett.*, **21**, e981, https://doi.org/10.1002/asl.981.

Madonna, E., C. Li, C. M. Grams, and T. Woollings, 2017: The link between eddy-driven jet variability and weather regimes in the North Atlantic–European sector. *Quart. J. Roy. Meteor. Soc.*, **143**, 2960–2972, https://doi.org/10.1002/qj.3155.

Masato, G., B. J. Hoskins, and T. Woollings, 2013: Winter and summer Northern Hemisphere blocking in CMIP5 models. *J. Climate*, **26**, 7044–7059, https://doi.org/10.1175/JCLI-D-12-00466.1.

Matsueda, M., and T. N. Palmer, 2018: Estimates of flow-dependent predictability of wintertime Euro-Atlantic weather regimes in medium-range forecasts. *Quart. J. Roy. Meteor. Soc.*, **144**, 1012–1027, https://doi.org/10.1002/qj.3265.

——, R. Mizuta, and S. Kusunoki, 2009: Future change in wintertime atmospheric blocking simulated using a 20-km-mesh atmospheric global circulation model. *J. Geophys. Res.*, **114**, D12114, https://doi.org/10.1029/2009JD011919.

Michelangeli, P.-A., R. Vautard, and B. Legras, 1995: Weather regimes: Recurrence and quasi stationarity. *J. Atmos. Sci.*, **52**, 1237–1256, https://doi.org/10.1175/1520-0469(1995)052<1237:WRRAQS>2.0.CO;2.

Moberg, A., and P. D. Jones, 2005: Trends in indices for extremes in daily temperature and precipitation in central and western Europe, 1901–99. *Int. J. Climatol.*, **25**, 1149–1171, https://doi.org/10.1002/joc.1163.

Molnos, S., T. Mamdouh, S. Petri, T. Nocke, T. Weinkauf, and D. Coumou, 2017: A network-based detection scheme for the jet stream core. *Earth Syst. Dyn.*, **8**, 75–89, https://doi.org/10.5194/esd-8-75-2017.

Oudar, T., J. Cattiaux, and H. Douville, 2020: Drivers of the northern extratropical eddy-driven jet change in CMIP5 and CMIP6 models. *Geophys. Res. Lett.*, **47**, e2019GL086695, https://doi.org/10.1029/2019GL086695.

Palmer, T. N., 1999: A nonlinear dynamical perspective on climate prediction. *J. Climate*, **12**, 575–591, https://doi.org/10.1175/1520-0442(1999)012<0575:ANDPOC>2.0.CO;2.

Peings, Y., J. Cattiaux, S. J. Vavrus, and G. Magnusdottir, 2018: Projected squeezing of the wintertime North-Atlantic jet. *Environ. Res. Lett.*, **13**, 074016, https://doi.org/10.1088/1748-9326/aacc79.

Perlwitz, J., T. Knutson, J. P. Kossin, and A. N. LeGrande, 2017: Large-scale circulation and climate variability. *Climate Science Special Report Fourth National Climate Assessment*, Vol. I, D. J. Wuebbles et al., Eds., U.S. Global Change Research Program, 161–184, https://doi.org/10.7930/J0RV0KVQ.5.1.

Piecuch, C. G., 2020: Likely weakening of the Florida Current during the past century revealed by sea-level observations. *Nat. Commun.*, **11**, 3973, https://doi.org/10.1038/s41467-020-17761-w.

Quagraine, K. A., B. Hewitson, C. Jack, I. Pinto, and C. Lennard, 2019: A methodological approach to assess the co-behavior of climate processes over southern Africa. *J. Climate*, **32**, 2483–2495, https://doi.org/10.1175/JCLI-D-18-0689.1.

Rahmstorf, S., J. E. Box, G. Feulner, M. E. Mann, A. Robinson, S. Rutherford, and E. J. Schaffernicht, 2015: Exceptional twentieth-century slowdown in Atlantic Ocean overturning circulation. *Nat. Climate Change*, **5**, 475–480, https://doi.org/10.1038/nclimate2554.

Reusch, D. B., R. B. Alley, and B. C. Hewitson, 2007: North Atlantic climate variability from a self-organizing map

perspective. *J. Geophys. Res.*, **112**, D02104, https://doi.org/10.1029/2006JD007460.

Richardson, A. J., C. Risien, and F. A. Shillington, 2003: Using self-organizing maps to identify patterns in satellite imagery. *Prog. Oceanogr.*, **59**, 223–239, https://doi.org/10.1016/j.pocean.2003.07.006.

Rikus, L., 2018: A simple climatology of westerly jet streams in global reanalysis datasets. Part I: Mid-latitude upper tropospheric jets. *Climate Dyn.*, **50**, 2285–2310, https://doi.org/10.1007/s00382-015-2560-y.

Robson, J., D. Hodson, E. Hawkins, and R. Sutton, 2014: Atlantic overturning in decline? *Nat. Geosci.*, **7**, 2–3, https://doi.org/10.1038/ngeo2050.

——, and Coauthors, 2018: Recent multivariate changes in the North Atlantic climate system, with a focus on 2005–2016. *Int. J. Climatol.*, **38**, 5050–5076, https://doi.org/10.1002/joc.5815.

Röthlisberger, M., and O. Martius, 2019: Quantifying the local effect of Northern Hemisphere atmospheric blocks on the persistence of summer hot and dry spells. *Geophys. Res. Lett.*, **46**, 10 101–10 111, https://doi.org/10.1029/2019GL083745.

Rousi, E., C. Anagnostopoulou, K. Tolika, and P. Maheras, 2015: Representing teleconnection patterns over Europe: A comparison of SOM and PCA methods. *Atmos. Res.*, **152**, 123–137, https://doi.org/10.1016/j.atmosres.2013.11.010.

——, H. W. Rust, U. Ulbrich, and C. Anagnostopoulou, 2020: Implications of winter NAO flavors on present and future European climate. *Climate*, **8**, 13, https://doi.org/10.3390/cli8010013.

Russo, S., and Coauthors, 2014: Magnitude of extreme heat waves in present climate and their projection in a warming world. *J. Geophys. Res. Atmos.*, **119**, 12 500–12 512, https://doi.org/10.1002/2014JD022098.

——, J. Sillmann, and E. M. Fischer, 2015: Top ten European heatwaves since 1950 and their occurrence in the coming decades. *Environ. Res. Lett.*, **10**, 124003, https://doi.org/10.1088/1748-9326/10/12/124003.

Saba, V. S., and Coauthors, 2016: Enhanced warming of the northwest Atlantic Ocean under climate change. *J. Geophys. Res. Oceans*, **121**, 118–132, https://doi.org/10.1002/2015JC011346.

Scaife, A. A., T. Woollings, J. Knight, G. Martin, and T. Hinton, 2010: Atmospheric blocking and mean biases in climate models. *J. Climate*, **23**, 6143–6152, https://doi.org/10.1175/2010JCLI3728.1.

Schaller, N., and Coauthors, 2016: Human influence on climate in the 2014 southern England winter floods and their impacts. *Nat. Climate Change*, **6**, 627–634, https://doi.org/10.1038/nclimate2927.

Schär, C., P. L. Vidale, D. Lüthi, C. Frei, C. Häberli, M. A. Liniger, and C. Appenzeller, 2004: The role of increasing temperature variability in European summer heatwaves. *Nature*, **427**, 332–336, https://doi.org/10.1038/nature02300.

Seneviratne, S. I., T. Corti, E. L. Davin, M. Hirschi, E. B. Jaeger, I. Lehner, B. Orlowsky, and A. J. Teuling, 2010: Investigating soil moisture–climate interactions in a changing climate: A review. *Earth-Sci. Rev.*, **99**, 125–161, https://doi.org/10.1016/j.earscirev.2010.02.004.

Shepherd, T. G., 2014: Atmospheric circulation as a source of uncertainty in climate change projections. *Nat. Geosci.*, **7**, 703–708, https://doi.org/10.1038/ngeo2253.

Sheridan, S. C., and C. C. Lee, 2011: The self-organizing map in synoptic climatological research. *Prog. Phys. Geogr.*, **35**, 109–119, https://doi.org/10.1177/0309133310397582.

Simpson, I. R., C. Deser, K. A. McKinnon, and E. A. Barnes, 2018: Modeled and observed multidecadal variability in the North Atlantic jet stream and its connection to sea surface temperatures. *J. Climate*, **31**, 8313–8338, https://doi.org/10.1175/JCLI-D-18-0168.1.

Skific, N., and J. Francis, 2012: Self-organizing maps: A powerful tool for the atmospheric sciences. *Applications of Self-Organizing Maps*, InTech, 251–268.

Stouffer, R. J., and Coauthors, 2006: Investigating the causes of the response of the thermohaline circulation to past and future climate changes. *J. Climate*, **19**, 1365–1387, https://doi.org/10.1175/JCLI3689.1.

Strommen, K., I. Mavilia, S. Corti, M. Matsueda, P. Davini, J. von Hardenberg, P. L. Vidale, and R. Mizuta, 2019: The sensitivity of Euro-Atlantic regimes to model horizontal resolution. *Geophys. Res. Lett.*, **46**, 7810–7818, https://doi.org/10.1029/2019GL082843.

Suarez-Gutierrez, L., W. A. Müller, C. Li, and J. Marotzke, 2020: Dynamical and thermodynamical drivers of variability in European summer heat extremes. *Climate Dyn.*, **54**, 4351–4366, https://doi.org/10.1007/s00382-020-05233-2.

Teng, H., and G. Branstator, 2019: Amplification of waveguide teleconnections in the boreal summer. *Curr. Climate Change Rep.*, **5**, 421–432, https://doi.org/10.1007/s40641-019-00150-x.

Totz, S., S. Petri, J. Lehmann, and D. Coumou, 2018: Regional changes in the mean position and variability of the tropical edge. *Geophys. Res. Lett.*, **45**, 12 076–12 084, https://doi.org/10.1029/2018GL079911.

Trenberth, K. E., 2011: Changes in precipitation with climate change. *Climate Res.*, **47**, 123–138, https://doi.org/10.3354/cr00953.

Ulbrich, U., J. G. Pinto, H. Kupfer, G. C. Leckebusch, T. Spangehl, and M. Reyers, 2008: Changing Northern Hemisphere storm tracks in an ensemble of IPCC climate change simulations. *J. Climate*, **21**, 1669–1679, https://doi.org/10.1175/2007JCLI1992.1.

Vallis, G. K., P. Zurita-Gotor, C. Cairns, and J. Kidston, 2015: Response of the large-scale structure of the atmosphere to global warming. *Quart. J. Roy. Meteor. Soc.*, **141**, 1479–1501, https://doi.org/10.1002/qj.2456.

van der Wiel, K., H. C. Bloomfield, R. W. Lee, L. P. Stoop, R. Blackport, J. A. Screen, and F. M. Selten, 2019: The influence of weather regimes on European renewable energy production and demand. *Environ. Res. Lett.*, **14**, 094010, https://doi.org/10.1088/1748-9326/ab38d3.

van Oldenborgh, G. J., and Coauthors, 2019: Human contribution to the record-breaking June 2019 heat wave in France. World Weather Attribution, 32 pp., https://www.worldweatherattribution.org/human-contribution-to-record-breaking-june-2019-heatwave-in-france/.

van Ulden, A. P., and G. J. van Oldenborgh, 2006: Large-scale atmospheric circulation biases and changes in global climate model simulations and their importance for climate change in central Europe. *Atmos. Chem. Phys.*, **6**, 863–881, https://doi.org/10.5194/acp-6-863-2006.

Vautard, R., 1990: Multiple weather regimes over the North Atlantic analysis of precursors and successors. *Mon. Wea. Rev.*, **118**, 2056–2081, https://doi.org/10.1175/1520-0493(1990)118<2056:MWROTN>2.0.CO;2.

——, P. Yiou, F. Otto, P. Stott, N. Christidis, G. J. van Oldenborgh, and N. Schaller, 2016: Attribution of human-induced dynamical and thermodynamical contributions in extreme weather events. *Environ. Res. Lett.*, **11**, 114009, https://doi.org/10.1088/1748-9326/11/11/114009.

Vogel, M. M., R. Orth, F. Cheruy, S. Hagemann, R. Lorenz, B. J. J. M. van den Hurk, and S. I. Seneviratne, 2017: Regional amplification of projected changes in extreme temperatures

strongly controlled by soil moisture–temperature feedbacks. *Geophys. Res. Lett.*, **44**, 1511–1519, https://doi.org/10.1002/2016GL071235.

Wang, Y., Z. Jiang, and W. Chen, 2015: Performance of CMIP5 models in the simulation of climate characteristics of synoptic patterns over East Asia. *J. Meteor. Res.*, **29**, 594–607, https://doi.org/10.1007/s13351-015-4129-4.

Ward, P. J., and Coauthors, 2018: Dependence between high sea-level and high river discharge increases flood hazard in global deltas and estuaries. *Environ. Res. Lett.*, **13**, 084012, https://doi.org/10.1088/1748-9326/aad400.

Wehrens, R., and J. Kruisselbrink, 2018: kohonen: Supervised and unsupervised self-organising maps. https://cran.r-project.org/web/packages/kohonen/index.html.

Woollings, T., 2010: Dynamical influences on European climate: An uncertain future. *Philos. Trans. Roy. Soc. London*, **368A**, 3733–3756, https://doi.org/10.1098/RSTA.2010.0040.

——, J. M. Gregory, J. G. Pinto, M. Reyers, and D. J. Brayshaw, 2012: Response of the North Atlantic storm track to climate change shaped by ocean–atmosphere coupling. *Nat. Geosci.*, **5**, 313–317, https://doi.org/10.1038/ngeo1438.

——, and Coauthors, 2018: Blocking and its response to climate change. *Curr. Climate Change Rep.*, **4**, 287–300, https://doi.org/10.1007/s40641-018-0108-z.

Yiou, P., and M. Nogaj, 2004: Extreme climatic events and weather regimes over the North Atlantic: When and where? *Geophys. Res. Lett.*, **31**, L07202, https://doi.org/10.1029/2003GL019119.

Zappa, G., L. C. Shaffrey, and K. I. Hodges, 2013: The ability of CMIP5 models to simulate North Atlantic extratropical cyclones. *J. Climate*, **26**, 5379–5396, https://doi.org/10.1175/JCLI-D-12-00501.1.

Zhu, C., and Z. Liu, 2020: Weakening Atlantic overturning circulation causes South Atlantic salinity pile-up. *Nat. Climate Change*, **10**, 998–1003, https://doi.org/10.1038/S41558-020-0897-7.